

1 **The effectiveness of solar radiation management for marine cloud brightening**
2 **geoengineering by fine sea spray in worldwide different climatic regions**

3
4 Zhe Song^{1*}, Shaocai Yu^{2,3*+}, Pengfei Li⁴⁺, Ningning Yao^{3,2}, Lang Chen^{3,2}, Yuhai Sun², Boqiong Jiang²,
5 Daniel Rosenfeld⁵

6
7 ¹ Research Center for Air Pollution and Health; Key Laboratory of Environmental Remediation and
8 Ecological Health, Ministry of Education, College of Environment and Resource Sciences, Zhejiang
9 University, Hangzhou, Zhejiang 310058, P.R. China

10 ² Zhejiang Province Key Laboratory of Solid Waste Treatment and Recycling; School of Environmental
11 Sciences and Engineering, Zhejiang Gongshang University, Hangzhou 310018, China

12 ³ School of Statistics and Mathematics, Zhejiang Gongshang University, Hangzhou 310018, China

13 ⁴ State Key Laboratory of Infrared Physics, Shanghai Institute of Technical Physics, Chinese Academy
14 of Sciences, Shanghai 200031, China

15 ⁵ Institute of Earth Sciences, The Hebrew University of Jerusalem, Jerusalem, Israel

16
17
18 *Equal contribution

19 ⁺ *Correspondence to:* Shaocai Yu (shaocaiyu@zjgsu.edu.cn), Pengfei Li (pengfeili@mail.sitp.ac.cn)

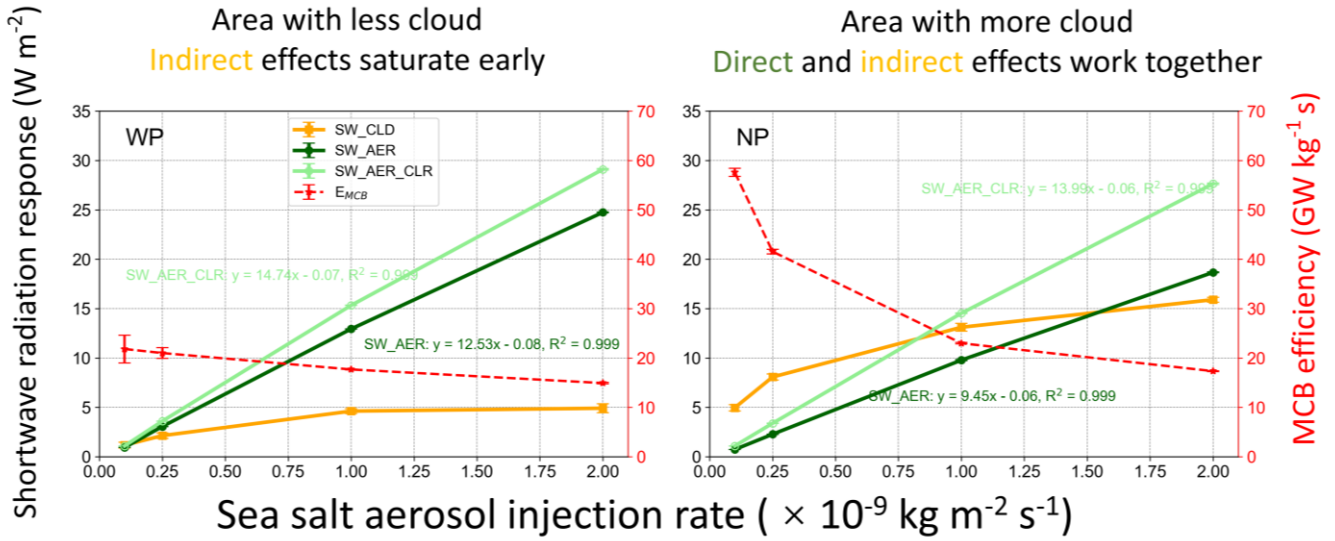
20
21 **To be submitted to**
22 **Atmospheric Chemistry and Physics**



Area with less cloud
Indirect effects saturate early



Area with more cloud
Direct and indirect effects work together



24

25

26 **Abstract**

27 Marine Cloud Brightening (MCB) geoengineering aims to inject aerosols over oceans to brighten
28 clouds and reflect more sunlight to offset the impacts of global warming or to achieve localized climate
29 cooling. There is still controversy about the contributions of direct and indirect effects of aerosols in
30 implementing MCB and the lack of quantitative assessments of both. Here, we design model simulations
31 with injected sea-salt aerosols in the same framework for five open oceans around the globe. Our results
32 show that a uniform injection strategy that does not depend on wind speed captures the sensitive areas of
33 the regions that produce the largest radiative perturbations during the implementation of MCB. When the
34 injection amounts are low, the sea-salt aerosols dominate the shortwave radiation mainly through the
35 indirect effects of brightening clouds, showing obvious spatial heterogeneity. As the indirect effect of
36 aerosols saturates with increasing injection rates, the direct effect increases linearly and exceeds the
37 indirect effects, producing a consistent increase in the spatial distributions of top-of-atmosphere upward
38 shortwave radiation. This study provides quantifiable radiation and cloud variability data for multiple
39 regional MCB implementations and suggests that injection strategies can be optimized by adjusting
40 injection amounts and selecting sensitive areas in the simulations of regional models.

41

42 **Keywords:** marine cloud brightening; solar radiation management; fine sea spray; climatic ocean regions;
43 geoengineering

44

45 **1. Introduction**

46 As global temperatures continue to rise, the international community is facing an unprecedented challenge
47 to achieve the ambitious goal set in the Paris Agreement of limiting global warming to within 1.5 °C
48 (Mengel et al., 2018). One of the key outcomes of the recently concluded 28th Conference of the Parties
49 (COP28) was the completion of the first Global Stocktake (GST), a mid-term assessment of the progress
50 made by countries toward achieving the climate goals of the Paris Agreement. However, the report
51 highlighted that current efforts to reduce emissions had fallen short of the intended targets
52 (<https://www.cop28.com/>). Against this backdrop, scientists are turning their attention to more innovative
53 geoengineering methods by attempting to reduce or offset the impacts of climate change through artificial
54 interventions in the climate (Visioni et al., 2023). Some geoengineering methods seek to capture or
55 remove CO₂ from the atmosphere to increase carbon sinks, while others focus on modifying solar
56 radiation, reducing incoming solar shortwave radiation, or reflecting more sunlight to cool the earth,
57 known as solar radiation management (SRM) (Lenton and Vaughan, 2009). Among these, marine cloud
58 brightening (MCB) has a certain realistic basis and is considered the most likely SRM method for regional
59 applications (Latham et al., 2014). It has been observed that exhaust emissions from ocean-going vessels
60 can lead to brighter clouds, with clear ship tracks also visible from satellites, and MCB aims to replicate
61 this effect by spraying sea-salt aerosols (Chen et al., 2012).

62 Aerosol-cloud interactions and their impacts on climate are complex (Rosenfeld et al., 2014, 2019).
63 Injected sea-salt aerosols affect clouds through indirect effects (Paulot et al., 2020). In the case of a
64 constant liquid water content, an increase in cloud droplet number concentration (CDNC) decreases the
65 cloud droplet size, increases the total surface area of cloud droplets, thereby enhancing the cloud albedo,
66 forming brighter clouds, and reflecting more sunlight back to space (the first indirect effect or Twomey
67 effect) (Twomey, 1974). At the same time, the decrease in cloud droplet size suppresses precipitation,
68 thereby increasing the cloud's lifespan and optical thickness (the second indirect effect of aerosols)
69 (Albrecht, 1989). Reducing the cloud drop size induces a faster evaporation and loss of cloud water.
70 However, the effect of the coarse sea spray aerosols has an opposite effect that offsets the loss of liquid
71 water path (Liu et al., 2022). In addition, those aerosols that are not injected into the clouds scatter more
72 sunlight back into space through the direct scattering effect (Ahlm et al., 2017; Partanen et al., 2012; Zhao
73 et al., 2021). Therefore, this method is also called marine sky brightening (MSB), which can work even
74 when there are no clouds. Here, we collectively refer to the practice of injecting sea-salt aerosols as MCB.

75 Compared to other geoengineering schemes, such as stratospheric aerosol injection (SAI), MCB has

76 unique advantages. For example, the sprayed aerosols have lower environmental risks and can be applied
77 locally to change the regional climate (Latham et al., 2008). Their deployment costs are relatively low
78 and flexible (Kravitz et al., 2014; Latham et al., 2012, 2014). However, despite these potential advantages,
79 the long-term effects and potential risks of MCB are not fully understood, and there are significant
80 uncertainties as well as ethical, political, and environmental risks. Therefore, most of the current
81 literatures examine the environmental and climate impacts of MCB implementation through modeling.

82 Table S1 summarizes the results of current modeling simulations on MCB with sea-salt aerosols, as
83 well as their implementation strategies. Most MCB studies use Earth-System Models to assess the impacts
84 of the implementation of MCB on climate. Early MCB studies assumed the effects of MCB
85 implementation by setting a fixed CDNC or directly modifying the cloud effective radius (r_e), ignoring
86 the processes such as generation, transport, dry and wet deposition, and activation of injected sea-salt
87 aerosols, and not including the direct radiative effect of aerosols. With the development of models,
88 researchers started to conduct more detailed studies by injecting aerosols or increasing sea-salt aerosol
89 emissions, taking into account the post-injection processes of aerosols mentioned above. The
90 implementation region of MCB is crucial. Existing studies have focused on the impacts of MCB
91 implementation in three key areas: open oceans globally, the equatorial region (between 30°S and 30°N),
92 and coastal areas with widespread marine stratocumulus clouds. Alterskjær et al. (2012) used the cloud-
93 weighted susceptibility function to find the most sensitive regions to the injection of sea-salt aerosols.
94 Similarly, Jones and Haywood (2012) determined the 10% of the marine regions globally most suitable
95 for implementing MCB through an iterative method. The contributions of direct and indirect effects of
96 aerosols during the implementation of MCB are still controversial and quantitative assessment of both is
97 lacking.

98 Here, we use the two-way coupled Weather Research and Forecasting - Community Multi-scale Air
99 Quality model (WRF-CMAQ), combined with previous studies on the region and injection strategies, to
100 implement MCB in five open oceans worldwide. This study simulates the regional radiation and cloud
101 responses caused by injecting sea-salt aerosols. This aims to explore the commonalities and differences
102 in MCB implementation in different regions and to seek the optimal strategy for MCB injection.

104 **2. Experiments and methods**

105 **2.1 Model configuration**

106 The two-way coupled WRF (v3.4) - CMAQ (v5.0.2) model that considers both direct and indirect effects

107 of aerosols was used in this study (Yu et al., 2014). In the two-way coupled model, aerosols predicted by
108 CMAQ are able to affect clouds, radiation, and precipitation simulated by WRF in a consistent online
109 coupled manner (Wong et al., 2012). Yu et al. (2014) further extended the two-way coupled WRF-CMAQ
110 model by incorporating the aerosol indirect effects (including the first, second, and glaciation aerosol
111 indirect effects), improving the ability of the WRF-CMAQ model to predict clouds and radiation. Wang
112 et al. (2021) validated this model.

113 The physical schemes of the WRF model are the same as those set in Yu et al. (2014), including the
114 asymmetric convective model (ACM2) for a planetary boundary layer (PBL) scheme (Pleim, 2007), the
115 Morrison 2-moment cloud microphysics scheme (Morrison et al., 2009), the Kain-Fritsch (KF2) cumulus
116 cloud parameterization, the Rapid Radiative Transfer Model for General Circulation Models (RRTMG)
117 longwave and shortwave radiation schemes, and the Pleim-Xiu (PX) land-surface scheme. The
118 meteorological initial and boundary conditions are provided by the National Center for Environmental
119 Prediction (NCEP) final analysis dataset (FNL) with a spatial resolution of $1^{\circ} \times 1^{\circ}$ and temporal resolution
120 of 6 h. The carbon bond gas-phase chemical mechanism (CB05) and aerosol module of AERO6 were
121 used in the CMAQ model. The anthropogenic emissions were taken from the Hemispheric Transport of
122 Air Pollution (HTAP_V2) projects (Janssens-Maenhout et al., 2015). The biogenic emissions were
123 estimated by the Biogenic Emissions Inventory System version 3.14 (BEISv3.14) model (Carlton and
124 Baker, 2011). Sea salt emissions were calculated online in CMAQ and were divided into open-ocean and
125 surf-zone emissions. In the open ocean, Gong (2003) extended the sea-salt aerosol parameterization of
126 Monahan et al. (1986) to submicron sizes, with the emission flux being linearly proportional to the ocean
127 area covered by whitecaps. CMAQ represents the atmospheric particle distribution as the superposition
128 of three log-normal modes, the Aitken, Accumulation, and Coarse modes (Binkowski and Roselle, 2003).
129 The particle size distribution and the geometric standard deviation of the emitted sea-salt aerosols are
130 adjusted to the local relative humidity before mixing with the ambient particle modes (Zhang et al., 2005).
131 The geometric mean diameter of accumulation mode sea-salt aerosols in the CMAQ ranged from 0.2651
132 to 0.8187 μm , with the geometric standard deviation constrained between 1.76 and 1.83. Surf-zone
133 emissions are calculated using the open ocean-source function of Gong (2003), with a fixed whitecap
134 coverage of 100% and a surf-zone width of 50 m. Kelly et al. (2010) provided a detailed description of
135 these processes. In the CMAQ model, the number concentration emission rate was calculated from the
136 mass emissions rate as follows:

$$E_{3n} = \left(\frac{6}{\pi}\right) \left(\frac{E_n}{\rho_n}\right) \quad (1)$$

$$E_0 = \frac{\sum_n E_{3n}}{D_{gv}^3 \exp\left(-\frac{9}{2} \ln^2 \sigma_g\right)} \quad (2)$$

where E_n was the mass emissions rate for species n and ρ_n was the density for that species. The sum $\sum_n E_{3n}$ was taken over all emitted species. The geometric mean diameter for mass or volume, D_{gv} , was given by $D_{gv} = D_g \exp(3 \ln^2 \sigma_g)$ from the Hatch-Choate relations for a lognormal distribution (Binkowski and Roselle, 2003). This study uses Geographic Information System software (ArcGIS) to obtain the open-ocean and surf-zone fractions for each grid within the modeling domain from shoreline information. The modeling domains of the five regions were almost entirely open ocean, with surf-zone fractions of less than 0.01%.

2.2 Experimental setup

As summarized in Table S1, the MCB geoengineering implementation areas included the globe, the equator (30°S–30°N), regions with extensive coverages of marine stratocumulus clouds, and so on. Therefore, based on previous experimental designs, we use the WRF-CMAQ model to simulate the injections of sea-salt aerosols in the five open ocean regions (Fig. 1c). These regions are WP and NP, located in the western and northern Pacific Ocean; Equa, located in the Philippine Sea along the equator; and SP and SA, located in the south Pacific and south Atlantic, respectively. The three regions, NP, SP and SA, are located along the western coast of continents, are considered to have extensive coverage of marine stratocumulus clouds and were the most suitable areas for implementing MCB (Alterskjær et al., 2012; Hill and Ming, 2012; Jones et al., 2009; Partanen et al., 2012; Stuart et al., 2013).

The grid numbers of WRF and CMAQ are 190×190 and 173×173, respectively, and both have a horizontal resolution of 12 km, with 29 vertical layers from the surface to about 21 km altitude. The simulation period for the WP, Equa, and NP regions in the northern hemisphere is from July 24, 2018, to September 1, 2018, while for the SP and SA regions in the southern hemisphere, the simulation period is from February 24, 2023, to April 1, 2023. The first 8 days of the model simulations are considered as the spin-up period to minimize the impacts of initial chemical conditions.

The results of the Base simulations with the model settings described above and default sea salt emissions (no aerosol injection) were obtained. As can be seen, there are significant differences in the cloud distributions for the five ocean regions in the Base simulations during the study period, with wider distributions of liquid clouds in the NP, SP, and SA regions, but fewer clouds in the WP and Equa regions

166 (Fig. 2, first column). Cloud heights are distributed between 500–2000 m, centered at 1000 m (Fig. S1,
 167 first column). The cloud fraction, CDNC, liquid water path (LWP), and sea-salt aerosol concentrations in
 168 the Base simulations for each region are summarized in Table 1.

169 We test four different sea-salt aerosol injection strategies, wind-speed-dependent **Natural×5**, **Wind-**
 170 **adjusted**, **Fixed at 10^{-9} kg m⁻² s⁻¹** and **Fixed-wind-adjusted**. All additional injected sea-salt aerosols are
 171 in the accumulation mode. In this study, the geometrical mean dry diameter of sea-salt aerosols injected
 172 into the five regions is about 0.11–0.15 μm, and is similar for all emission scenarios.

173 **Natural×5**: Increase the emission rates of accumulation mode sea-salt aerosols by a factor of 5 (Hill
 174 and Ming, 2012). This is a simple wind-speed-dependent increase. The injection rates in the five regions
 175 are equivalent to $0.031\text{--}0.085 \times 10^{-9}$ kg m⁻² s⁻¹ (Table S2).

176 **Wind-adjusted**: Salter et al. (2008) designed a spray vessel for injecting sea-salt aerosols with a
 177 spray efficiency that was dependent on wind speed and was expected to achieve maximum spray outputs
 178 at wind speeds between 6–8 m s⁻¹. The threshold wind speed was set to 7 m s⁻¹ and the spray efficiency
 179 at lower wind speeds raised to the power of 1.5. We use the source function of Partanen et al. (2012) as
 180 follows, where u is the 10 m wind speed. For example, at wind of 7 m s⁻¹ the injection rate will be $0.26 \times$
 181 10^{-9} kg m⁻² s⁻¹.

$$182 \quad F_{m, \text{baseline}} = \begin{cases} 5 \times 2.8 \times 10^{-12} \times \left(\frac{u}{1 \text{ m s}^{-1}}\right)^{1.5} \text{ kg m}^{-2}\text{s}^{-1}, & u < 7 \text{ m s}^{-1} \\ 5 \times 2.8 \times 10^{-12} \times 7^{1.5} \text{ kg m}^{-2}\text{s}^{-1}, & u \geq 7 \text{ m s}^{-1} \end{cases} \quad (3)$$

183 **Fixed at 10^{-9} kg m⁻² s⁻¹**: Unlike the previous two injection methods, the injections of sea-salt aerosols
 184 at a fixed rate of 10^{-9} kg m⁻² s⁻¹ are not dependent on wind speed and increased uniformly over all ocean
 185 grids. Injecting sea-salt aerosols at a fixed rate identified the geographic areas that were most sensitive to
 186 increased sea-salt aerosols and produced the largest top-of-atmosphere (TOA) radiative perturbations
 187 (Alterskjær et al., 2012). Many other studies have used this method (Goddard et al., 2022; Horowitz et
 188 al., 2020; Mahfouz et al., 2023). Uniform injections of sea-salt aerosols throughout the region ignored
 189 aerosol transports and dispersion at the boundary. Therefore, based on the results of a fixed 10^{-9} kg m⁻² s⁻¹
 190 injection rate, we identify the geographical regions (30×50 grid points, approximately 360 km \times 600
 191 km, away from the domain boundary) in five ocean areas where the TOA radiative perturbations caused
 192 by uniform injection are the largest, and the most sensitive. Table S3 shows the locations of these sensitive
 193 regions. The injection amount in the sensitive region at a fixed 10^{-9} kg m⁻² s⁻¹ injection rate is found to be
 194 about 1/20 of those in the full domain.

195 **Fixed-wind-adjusted**: To rule out differences in radiative and cloud response due to wind

196 variabilities on spray rates, we perform an additional adjustment. Similar to **Natural×5**, the injections of
197 sea-salt aerosols were also dependent on the wind speed but the integrated amounts in the region are set
198 to be equal to the case that all area had a fixed rate of $10^{-9} \text{ kg m}^{-2} \text{ s}^{-1}$ (**Fixed**).

199 **2.3 Calculations**

200 The calculation method related to radiation, cloud properties, and cloud radiation forcing is based on
201 Goddard et al. (2022), briefly described here as follows. This study focuses on the shortwave radiative
202 flux responses at the TOA due to the injections of sea-salt aerosols, which is consistent with the definition
203 of effective radiation forcing (ERF) (Forster et al., 2007). The sea surface temperature in the model is
204 preset by NCEP-FNL, so the model's surface temperature and upward longwave radiation would not
205 respond to the increased sea-salt aerosols. The total upward shortwave radiation flux (SW_TOT) at the
206 TOA is under the all-sky conditions. The responses of SW_TOT to the injections of sea-salt aerosols
207 could be divided into the cloud radiation effects (SW_CLD, excluding the direct effect of the aerosols)
208 and direct scattering effects when clouds are present (SW_AER).

$$209 \quad \text{SW_TOT} = \text{SW_CLD} + \text{SW_AER} \quad (4)$$

210 The diagnosis of CLEAN-SKY (no aerosols) is not considered in the previous WRF-CMAQ model.
211 So in this study, we extend this feature in the WRF-CMAQ model using the methodology of Ghan et al.
212 (2012) by performing a double radiative call at each time step to calculate radiation variables related to
213 CLEAN-SKY (SW_CLD). We also study the impacts of injecting sea-salt aerosols on the upward
214 shortwave radiation flux at the TOA under the clear-sky conditions (SW_AER_CLR). At this time, only
215 the direct scattering effect of aerosols existed, which is considered to be the maximum MSB potential
216 generated by injecting sea-salt aerosols when there is no cloud.

217 Due to the different amounts of sea-salt aerosols injected in different ways, it results in different
218 SW_TOT responses. Therefore, we propose the concept of MCB efficiency (E_{MCB}) to measure the
219 relationships between the amount of sea-salt aerosol injections and the resulting radiation flux responses
220 (Table S2).

$$221 \quad E_{MCB} = \frac{\text{SW_TOT response due to injection of sea-salt aerosol (W m}^{-2}\text{)}}{\text{Sea-salt aerosol injections (kg m}^{-2} \text{ s}^{-1}\text{)}} \quad (5)$$

222 This is a measure of the mass efficiency of MCB implementing in different regions, that is, how much
223 SW_TOT responses are expected to be generated by injecting sea-salt aerosols at a rate of $1 \text{ kg m}^{-2} \text{ s}^{-1}$.
224 $E_{MCB} = 1$ means that injecting 1 kg of sea-salt aerosols per unit time in the current study area is expected

225 to produce a 1 GW (10^9 W) SW_TOT response. Note that this value (E_{MCB}) is based on model calculations
 226 under specific atmospheric conditions within the study region and is only used to analyze the sensitivities
 227 of the radiative flux to different injection methods and injection amounts.

228 This study focuses on the changes in liquid clouds and evaluate the responses in cloud condensation
 229 nuclei (CCN), cloud fraction, CDNC, r_e , LWP, cloud optical thickness (COT), and cloud albedo due to
 230 the injections of sea-salt aerosols. These calculations are shown in Supplementary Text S1.

231 Cloud radiation forcing (CRF) parameters can be used to quantify the responses of SW_CLD to
 232 changes in cloud cover or cloud albedo, defined as follows (Goddard et al., 2022):

$$233 \quad \text{CRF}_{param} = \alpha_c f \quad (6)$$

234 where α_c is mean cloud albedo and f is mean cloud fraction.

235 The CRF parameters can be approximated using the perturbation method as follows (Goddard et al.,
 236 2022):

$$237 \quad \text{CRF}'_{param} = \alpha'_c \bar{f} + \bar{\alpha}_c f' + \alpha'_c f' \quad (7)$$

238 where the first term on the right-hand side indicates the changes in CRF_{param} driven by the perturbation
 239 of cloud albedo, the second term indicates the changes driven by the perturbation of cloud fraction, and
 240 the third term denotes the changes driven by the interactions of the two. The horizontal bars on α_c and f
 241 are defined as the monthly means of the Base, and the prime (') defines the monthly mean differences
 242 between the sensitivity experiments and Base. The fourth column of Fig. S23 shows that the differences
 243 between CRF_{param} and CRF'_{param} are small enough that the perturbation method can be used to
 244 approximate the CRF'_{param} .

245 The changes in cloud albedo are driven by multiple processes. Based on Quaas et al. (2008) and
 246 Christensen et al. (2020), Goddard et al. (2022) established the following equation to assess the relative
 247 effects of CDNC, LWP, and mean cloud fraction on the responses of SW_CLD due to the injections of
 248 sea-salt aerosols:

$$249 \quad \frac{\Delta \alpha}{\Delta \ln \text{AOD}} = f \Delta \alpha_c (1 - \alpha_c) \left(\frac{1}{3} \frac{\Delta \ln \text{CDNC}}{\Delta \ln \text{AOD}} + \frac{5}{6} \frac{\Delta \ln \text{CLWP}}{\Delta \ln \text{AOD}} + \frac{\Delta \ln f}{\Delta \ln \text{AOD}} \right) \quad (8)$$

250 where α is the planetary albedo, Δ represents the difference in monthly average results between
 251 sensitivity experiments and Base simulations, and α_c is the cloud albedo. The three terms inside the right
 252 parenthesis represent the relative contributions of Twomey effect, LWP effect, and cloud fraction effect,
 253 respectively, with the latter two related to the second aerosol indirect effect (Albrecht, 1989).

254 The perturbations by generating three ensemble members for each experiment in each region were

255 added. The results of all sensitivity experiments are compared to those of Base simulations. Unless
256 otherwise specified, all results in this study are shown as overall regional monthly averages of the
257 ensemble.

258

259 **3. Results**

260 **3.1 The impacts of different injection strategies on shortwave radiation at the TOA.**

261 In modeling studies, variations in methods used to increase sea-salt aerosols may lead to different
262 conclusions, and these variations may be one of the reasons for differences in the assessments of MCB
263 potentials in the previous studies. In this study, sea-salt aerosols injected in different strategies (with dry
264 diameters of about 0.11–0.15 μm , Fig. 1a) increase the SW_TOT at the TOA by 0.07–25 W m^{-2} in the
265 five ocean regions (Fig. 3a). The Natural \times 5 and Wind-adjusted strategies, which rely on wind speeds,
266 inject sea-salt aerosols of 0.031–0.085 and 0.18–0.21 $\times 10^{-9} \text{ kg m}^{-2} \text{ s}^{-1}$ into the five regions, respectively,
267 and result in SW_TOT variations of 0.07–2.1 and 1.4–8.4 W m^{-2} , respectively (Fig. 3a and Table 2).
268 Uniformly injections of sea-salt aerosols at a fixed rate of $10^{-9} \text{ kg m}^{-2} \text{ s}^{-1}$ results in SW_TOT changes of
269 11–25 W m^{-2} in the five regions. The three continental west coast stratocumulus regions of NP, SP, and
270 SA have the most significant SW_TOT responses, all exceeding 20 W m^{-2} , while the SW_TOT responses
271 in the WP and Equa regions are 18 and 11 W m^{-2} , respectively.

272 Injecting the same amount of sea-salt aerosols results in substantial variations in SW_TOT responses
273 across the different regions (Fig. S2). The sea-salt aerosols sprayed in the Fixed-wind-adjusted
274 experiments are also dependent on wind speed, but the amount of emission rate integrated in the full
275 domain is consistent with the fixed rate of $10^{-9} \text{ kg m}^{-2} \text{ s}^{-1}$, ruling out the differences caused by the amount
276 of injected sea-salt aerosols. Although both strategies inject the same amounts of sea-salt aerosols, the
277 SW_TOT responses they produce are significantly different. The Fixed-wind-adjusted strategy results in
278 SW_TOT changes of 5.0–20 W m^{-2} in the five regions (Fig. 3a), indicating that the shortwave radiation
279 flux changes caused by wind-speed-dependent injections are smaller than those caused by uniformly
280 injections, and showed regional differences.

281 Figure 3b shows the E_{MCB} values of different sea-salt injection strategies in the five regions. Overall,
282 MCB implementation is more efficient in the NP, SP, and SA regions, while it is less efficient in the WP
283 and Equa, which is similar to the previous SW_TOT response results. E_{MCB} also varies for different
284 injection strategies. In the NP, SP, and SA regions, the E_{MCB} values of the Natural \times 5 and Wind-adjusted

285 strategies with relatively small injection amounts are higher than the other two strategies with large
286 injection amounts. At the same injection amount, injecting at a fixed rate shows higher E_{MCB} relative to
287 injections depending on wind speed, as consistently shown in all five regions (Fig. 3b). Since the number
288 flux of aerosols increased with the decreases of the injected aerosol particle size for the same mass flux,
289 we examined the MCB efficiency in units of aerosol number concentration (Fig. S3). The results show
290 that the number efficiency of MCB is proportional to the injection rate of aerosol number (Fig. S3c). In
291 the same quality injected, the aerosol number varies greatly (Fig. S3d).

292 The productions of sea-salt aerosols in nature are strongly correlated with wind speed, and most
293 models associated sea-salt aerosol emissions with wind speed (Ahlm et al., 2017; Grythe et al., 2014).
294 Injection strategies depending on wind speed make the distributions of added sea-salt aerosols closer to
295 the natural distributions. In natural environments, sea-salt aerosol emissions in strong-wind areas (e.g.,
296 storm or typhoon areas) and surf zones are usually much larger than in weak-wind areas. Therefore,
297 injection strategies depending on wind speed concentrate the added sea-salt aerosols in strong-wind areas
298 and surf zones, while the weak-wind regions increase relatively little sea-salt aerosols (Fig. S4). Injecting
299 uniformly at a fixed rate in the model will result in a large increase of sea-salt aerosols in places with
300 originally low aerosol concentrations (e.g., weak-wind regions). Therefore, when using models to
301 simulate the injections of sea-salt aerosols by increasing the emission rate, it is necessary to consider the
302 impacts of different injection methods on the distributions of sea-salt emissions. Using a uniformly
303 increasing method independent of wind speed can not only avoid the situation of a smaller increase in
304 sea-salt emissions in regions with lower wind speeds, but can also identify the geographical areas most
305 sensitive to the increased sea-salt aerosols and producing the largest TOA radiation perturbations
306 (Alterskjær et al., 2012).

307 Injecting sea-salt aerosols in the sensitive areas with the same uniform injections ($10^{-9} \text{ kg m}^{-2} \text{ s}^{-1}$, the
308 injection rate is about 1/20 of the full domain injection) results in changes of $0.49\text{--}3.4 \text{ W m}^{-2}$ in SW_TOT
309 in the five ocean regions (Table S2). The SW_TOT responses are the largest in the SP region, at 3.4 W m^{-2} ,
310 and 2.7 and 1.7 W m^{-2} in the NP and SA regions, respectively, while they were only 0.49 and 0.83 W m^{-2}
311 in the WP and Equa regions, respectively. The injected sea-salt aerosols produced SW_TOT changes
312 of $5.11\text{--}14.3 \text{ W m}^{-2}$ in the sensitive areas (Fig. 1b). Similarly, the increases in SW_TOT in the SP, SA,
313 and NP regions all exceeded 9 W m^{-2} , with the highest in the SP region at 14.3 W m^{-2} . In the WP and Equa
314 regions, although the increases in SW_TOT are only 5.11 and 5.26 W m^{-2} , respectively. Considering that
315 the original intents of MCB or MSB design are regional application (hurricane mitigation, coral reef

316 protection and polar sea ice recovery) (Latham et al., 2014), choosing to inject sea-salt aerosols in the
317 sensitive areas could achieve the corresponding cooling goals within the region, and also affected larger
318 areas through the diffusions and transports of aerosols.

319 **3.2 Characterization of the radiation responses.**

320 SW_TOT responses are defined as the sum of the upward shortwave radiation flux response at the TOA
321 generated by the combined effects of the direct scattering effect of aerosols (SW_AER) and cloud
322 radiative effect (SW_CLD) after injecting sea-salt aerosols. Figure 4 shows the contributions of SW_AER
323 and SW_CLD responses in the SW_TOT produced by different injection strategies in the five ocean
324 regions. The majority of the SW_TOT radiative flux response due to the lower mass injection Natural×5
325 and Wind-adjusted strategies is caused by the SW_CLD response (Fig. 4a). In the NP, SP, and SA regions,
326 the contributions of SW_CLD exceed 70%, suggesting that sea-salt aerosols injected at these locations
327 increase the SW_TOT mainly by affecting clouds through indirect effects. In the Equa, the responses of
328 SW_TOT are entirely caused by SW_AER. The proportion of SW_AER produced by the uniform
329 injection of sea-salt aerosols at a fixed rate of 10^{-9} kg m⁻² s⁻¹ continued to increase (Fig. 4c). In the WP,
330 Equa, and SP regions, the proportion of SW_AER exceeded that of SW_CLD. In the SA region, SW_CLD
331 and SW_AER are almost equal, while in the NP region, the SW_CLD response is 13 W m⁻², still greater
332 than SW_AER (9.8 W m⁻²). This is because there is a saturation phenomenon in the cloud response to
333 aerosols injections (discussed below), and the NP, SP, and SA regions provide more SW_CLD responses,
334 while the cloud responses in the WP and Equa regions saturate and no longer increase. The results of
335 Fixed-wind-adjusted case show that, at the same injection amount, the SW_AER responses caused by the
336 injection strategy relying on wind speed is significantly smaller than those of the method with fixed-rate
337 uniform injection, while the disparity in SW_CLD responses is minimal. This is because the injection
338 strategy relying on wind speed distributed most of the increased sea-salt aerosols to areas with already
339 high emissions, such as strong-wind areas and surf zones, where the excess marine aerosols have already
340 saturated the cloud responses, resulting in minor changes in SW_CLD. In areas with weak winds, the
341 potentials for direct aerosol scattering are not fully exploited due to the relatively small amounts of sea-
342 salt aerosols injected, leading to a lower SW_AER response.

343 Figures S5 and S6 show the spatial distributions of SW_CLD and SW_AER responses resulting from
344 different injection methods in the five ocean regions. The SW_CLD responses are stronger in the three
345 regions of NP, SP, and SA, while they are weaker in the regions of WP and Equa, and in some grids they

346 even lead to a reduction of the upward shortwave radiation (Fig. S5). The spatial distributions of the
347 SW_CLD responses exhibit noticeable discontinuity, reflecting significant regional differences in the
348 non-uniform distributions of clouds and their impacts on shortwave radiation at the TOA. The effect of
349 cloud properties on SW_CLD will be shown in Section 3.5. Due to the influences of various complex
350 factors on cloud formations and distributions, simulation results related to clouds show significant spatial
351 variabilities. This might be the result of the combined effects of local meteorological conditions and
352 changes in cloud physical properties caused by sea-salt aerosol injections.

353 In contrast, the spatial distributions of the SW_AER response are smoother, leading to consistent
354 increases in upward shortwave radiation at the TOA in all ocean regions (Fig. S6). This indicates smaller
355 spatial limitations in the distributions of aerosol particles, allowing direct scattering effects to take place
356 everywhere. The direct scattering effect of aerosols is primarily related to the concentrations and physical
357 properties of the particles (discussed below), unlike clouds, which are influenced by multiple variables.
358 These results suggest that when implementing geoengineering measures, it is essential to
359 comprehensively consider the interactions between aerosols and clouds, as well as their different response
360 patterns in various regions. Furthermore, the high spatial variabilities of cloud radiation effects emphasize
361 the need for improved resolution in future model studies of cloud-aerosol interactions.

362 The SW_CLD response resulting from the injection of sea-salt aerosols in the sensitive areas of five
363 ocean regions exhibits significant spatial differences. The SW_CLD response is larger than the SW_AER
364 response in the sensitive areas of NP, SP, and SA, indicating that the changes in SW_TOT are mainly
365 driven by the cloud radiation response (Fig. 5). In contrast, the SW_CLD response is smaller in the WP
366 and Equa regions. This regional difference is similar to that observed with uniform injection across the
367 entire region. The SW_AER response shows consistent results in all areas, resulting in a radiation
368 response change of 3.58–5.44 W m⁻² within the injection areas. In the WP and Equa, the variations in
369 SW_TOT are primarily driven by the direct scattering effects of aerosols. Aerosols can have a greater
370 impact on radiation responses outside the sensitive areas through transports and diffusions, reaching up
371 to three times the total radiation within the sensitive areas (Fig. 6). In all regions except WP, the total
372 SW_CLD response outside the sensitive region was about 270%–408% higher than inside. In WP, the
373 SW_CLD response outside the sensitive area has a negative effect. The SW_CLD responses in NP, SP,
374 and SA extend to the west and northwest of the injection by the prevailing winds, indicating that clouds
375 in these areas are affected by the injection of sea-salt aerosols (Fig. 5). Changes in cloud microphysical
376 properties will be presented later. The SW_CLD variations in other directions are not uniform, and there

377 is negative SW_CLD responses in some grids, which again reflects the spatial complexities of cloud
378 radiation effects. The direct scattering effects of aerosols on areas outside the sensitive region is reflected
379 in a widespread increase in upward shortwave radiation at the TOA. The total SW_AER responses outside
380 the sensitive areas in the five ocean regions are approximately 160%–281% higher than inside, but lower
381 than the impacts of SW_CLD responses outside the sensitive areas. There are consistencies in the spatial
382 distributions of SW_AER and SW_CLD responses.

383 **3.3 Saturation of the cloud radiative responses.**

384 Figure 7 shows that under low levels of sea-salt aerosol injections, radiation response changes are mainly
385 driven by SW_CLD responses. As the injected sea-salt aerosols increased, the SW_CLD responses
386 gradually reach saturation. After reaching a certain injection level, the increases of SW_CLD responses
387 stabilize at its maximum value and no longer increases with further injections. The SW_CLD responses
388 show large differences in the five ocean regions, and the different shapes and slopes of the curves indicate
389 that the cloud radiative forcing responses to the sea-salt aerosol injections are different in each region.
390 This might be due to variations in cloud types, cloud amounts, and atmospheric conditions in the different
391 regions. In the NP, SP, and SA, the SW_CLD responses exceed 10 W m^{-2} , while in WP, it saturates at 5
392 W m^{-2} . In Equa, when the sea-salt aerosol injection rate is $10^{-9} \text{ kg m}^{-2} \text{ s}^{-1}$, the SW_CLD response is 0.5
393 W m^{-2} , and even when the injection doubled, the SW_CLD response remains at 0.5 W m^{-2} . This implies
394 that the SW_TOT at Equa was almost exclusively from the contributions of the direct scattering effects
395 of aerosols.

396 In contrast to SW_CLD, the SW_AER responses increase linearly with the injections of sea-salt
397 aerosols ($R^2 > 0.99$). As the injection increases, the contributions of SW_AER to SW_TOT gradually
398 increase, surpassing the SW_CLD responses, and show the same trends across the five regions. This
399 implies that at higher injection levels, the contributions of SW_CLD to total radiation change saturated,
400 and cloud properties no longer significantly change. At this point, sea-salt aerosols primarily affect
401 radiation through direct scattering effects, and the aerosol particles' ability to scatter solar radiation
402 continues to increase with the increases in aerosol quantities. In some cloud-free regions or weather
403 conditions, injected sea-salt aerosols are still able to function through direct scattering.

404 There exists a specific injection level at which the SW_CLD and SW_AER responses are equal. In
405 the NP region, when the injection level is approximately $1.55 \times 10^{-9} \text{ kg m}^{-2} \text{ s}^{-1}$, both SW_CLD and
406 SW_AER responses are 15 W m^{-2} . In the SP and SA, these levels are about $0.67 \times 10^{-9} \text{ kg m}^{-2} \text{ s}^{-1}$ and 1×10^{-9}

407 $^9 \text{ kg m}^{-2} \text{ s}^{-1}$, respectively. While in WP, the responses were already equal when the injection amount was
408 $0.15 \times 10^{-9} \text{ kg m}^{-2} \text{ s}^{-1}$. Since there is a saturation of the cloud radiation effects, E_{MCB} decreases with the
409 increases in sea-salt aerosol injection amounts (Fig. 7, red dashed line). This can also explain the higher
410 E_{MCB} of the Natural $\times 5$ and Wind-adjusted strategies with relatively low injection amounts (Fig. 3b).
411 Therefore, wind-dependent injection strategies lead to the injection of large amounts of sea-salt aerosols
412 in certain areas with high wind speeds, leading to saturation of cloud radiation effects, which might affect
413 the performances of MCB in the simulations of regional and global models.

414 When less sea-salt aerosols are injected, both SW_CLD and SW_AER responses contribute to the
415 changes of SW_TOT. As the injection amounts increase, the SW_CLD responses saturate, and the
416 increases in SW_TOT depends on the increases in SW_AER responses, leading to a decrease in E_{MCB}
417 (Fig. 7) Therefore, implementing geoengineering with sea-salt aerosol injections requires considering
418 local atmospheric conditions and balancing the relationships between cooling goals and sea-salt injection
419 efficiencies.

420 Under clear and cloudless conditions, injecting sea-salt aerosols could still increase the SW_TOT
421 through direct scattering, and this effect exceeds those of aerosol direct scattering when clouds are present.
422 The variation of the upward shortwave radiation flux at the TOA under the clear-sky conditions
423 (SW_AER_CLR) does not exhibit significant regional heterogeneity across the ocean areas (Figs. 5 and
424 S7), suggesting that the contribution of direct aerosol scattering is more uniform globally when
425 considering the effects of sea-salt injections on the Earth's radiation budget. The SW_AER_CLR
426 responses are also linearly correlated with the injection of sea-salt aerosols ($R^2 > 0.99$), and it exceeds the
427 SW_AER responses (Fig. 7). This is because cloud layers also scatter and absorb solar radiation, so this
428 scattering effect is more significant under clear sky conditions. It is reflected that in regions with strong
429 cloud radiation effects, such as the NP, SP, and SA regions, the differences between the SW_AER and
430 SW_AER_CLR responses are also larger (Fig. 7). When injecting sea-salt aerosol in sensitive areas, the
431 spatial distributions of SW_AER_CLR and SW_AER responses are highly consistent (Fig. 5). Therefore,
432 injecting sea-salt aerosol under conditions of low cloud covers or clear skies also increases the upward
433 shortwave radiation flux at the TOA.

434 **3.4 Factors affecting the radiation effects.**

435 Uniform injections of $10^{-9} \text{ kg m}^{-2} \text{ s}^{-1}$ sea-salt aerosols lead to an increase in aerosol optical depth (AOD)
436 of 0.20–0.37 in all regions (Fig. 8). The distributions of AOD within the regions are not uniform due to

437 aerosol transports and diffusions, with some areas showing an increase in AOD of over 0.6. Injecting sea-
438 salt aerosols in sensitive areas lead to an AOD increase of 0.077–0.12, while outside the injection areas,
439 AOD gradually decreases as the aerosols transport and disperse. With the increases in sea-salt aerosol
440 injections, AOD shows a linear increase within a certain range in all five ocean regions ($R^2 > 0.997$, Fig.
441 9a). There is a strong correlation between the AOD changes caused by sea-salt injection and the SW_AER
442 responses. When sea-salt aerosols are uniformly injected across the entire region, the correlation
443 coefficients between AOD and SW_AER responses in the five ocean areas are greater than 0.94, and
444 when injected in sensitive areas, the correlation coefficients are greater than 0.99 (Fig. S8). The optical
445 properties of injected aerosols are described in Supplementary Text S2. In general, the injected sea-salt
446 aerosols scatter sunlight more efficiently than absorb it, causing solar radiation to be reflected back into
447 space and tend to scatter more uniformly or backward rather than forward.

448 In the regions with higher cloud cover, such as NP, SP, and SA, injected sea-salt aerosols significantly
449 increases cloud fraction (Fig. 2, third column and Table 1), leading to the formations of more clouds or
450 expanding the coverage, vertical thickness and lifetime of existing clouds (Goddard et al., 2022). The
451 injection of sea-salt aerosols in sensitive areas have similar results, where cloud fractions increase both
452 inside the injection areas and in the regions affected by aerosol transports and diffusions (Fig. S13).
453 Taking the SP region as an example, Fig. 10 demonstrates that uniformly injections of $10^{-9} \text{ kg m}^{-2} \text{ s}^{-1}$ sea-
454 salt aerosols significantly increases the CDNC. More cloud droplets capture more water vapor, leading to
455 an increase in LWP. Additionally, the increases in cloud thickness also contribute to the increase in LWP.
456 The increase in CDNC decreases the mean r_e by $8.9 \mu\text{m}$ ($\sim -37\%$), increases the COT by more than 220%,
457 and ultimately increases the mean cloud albedo over the region by 0.19 ($\sim 64\%$). Similarly, injecting sea-
458 salt aerosols in the NP and SA regions lead to average cloud albedo increases of 0.17 and 0.20, respectively,
459 while in the WP and Equa, the increases are 0.15 and 0.13, respectively (Figs. S14–S17). The injection of
460 sea-salt aerosols within the sensitive areas has less effect on cloud microphysical properties than the whole
461 region injections. This is because when sea-salt aerosols are injected across the entire region, the
462 surrounding sea-salt aerosols affect the sensitive areas through transports, resulting in an enhanced
463 cumulative effect on cloud microphysical properties in the sensitive areas. Injecting sea-salt aerosol in
464 the sensitive area of the SP affected clouds in the surrounding region through transports, increases the
465 average cloud albedo across the entire area by 0.032 over the entire region and by 0.12 within the sensitive
466 regions, which is less than the effects of injection across the entire area (Fig. S18). Similarly, injecting
467 sea-salt aerosols in the sensitive areas of other ocean regions lead to average cloud albedo increases of

468 0.015–0.024 across the entire area, with increases of 0.11 in the sensitive areas of the SP and SA regions,
469 and increases of 0.090 and 0.10 in the WP and Equa, respectively (Figs. S19–S22).

470 **3.5 Drivers of SW_CLD responses.**

471 The cloud radiation forcing (CRF) parameters are used to calculate the effects of changes in cloud cover
472 and cloud albedo on the SW_CLD responses due to the injections of sea-salt aerosols. Figure S23
473 illustrates the increase in the CRF parameter coinciding with the increases in the SW_CLD responses
474 after uniform injection of sea-salt aerosols in the five regions (Fig. S5, third row). The results are similar
475 for injections in the sensitive areas (Fig. S24, third column, and Fig. 5, first column). The CRF'_{param}
476 calculated using the perturbation method indicates that in the five ocean regions, CRF'_{param} is primarily
477 driven by perturbations in cloud albedo (Fig. S25, first column), and it significantly surpasses the changes
478 in cloud fractions and their interactions. Cloud albedo changes explain over 70% of the CRF'_{param} in all
479 five regions except the Equa. The contribution of cloud fraction changes ranges from 13.9% to 23.7%,
480 while the interactions between the two factors account for only about 10% (Fig. S25, second and third
481 columns). The results are similar for injections in sensitive regions, where changes in cloud albedo
482 account for 58.8%–99.4% of the CRF'_{param} , followed by changes in cloud fractions, with the smallest
483 contributions from their interactions (Fig. S26).

484 Figure 11 evaluates the relative effects of Twomey, LWP, and cloud fractions on the SW_CLD
485 responses after uniformly injecting sea-salt aerosols in five ocean regions. The results indicate that
486 changes in CDNC (Twomey effect) and LWP are the main drivers of SW_CLD responses, while changes
487 in cloud fraction contribute minimally to the SW_CLD responses. Except for the Equa region, changes
488 in CDNC and LWP account for 48.4%–52.5% and 39.0%–41.7% of the SW_CLD changes, respectively,
489 with cloud fraction changes contributing to less than 10.0% (Fig. 11). The results are similar for injections
490 in sensitive areas, with changes in CDNC and LWP contributing similarly and more than changes in cloud
491 fractions to SW_CLD (Fig. S27). The changes in SW_CLD responses after aerosol injections in the
492 sensitive areas of Equa are mainly contributed by LWP effects (~70%).

493 Uniform injections of sea-salt aerosols at a rate of 10^{-9} kg m⁻² s⁻¹ produce susceptibilities ($\frac{\Delta\alpha}{\Delta \ln AOD}$)
494 ranging from 0.00030 to 0.0035 in the five regions, with corresponding spatial distributions shown in Fig.
495 11. NP, SP, and SA regions exhibit cloud responses that are more sensitive to aerosol injections in most
496 of the region, with susceptibilities ranging from 0.0028 to 0.0035. The Equa shows the lowest
497 susceptibility, indicating that the system is less responsive to variations in aerosol injections. It is

noteworthy that although the average susceptibility in the WP region is 0.0013, the higher susceptibility values are concentrated in the north of 35°N, where the average susceptibility is 0.0026, similar to those of the SP region, suggesting that clouds here are more susceptible to aerosol injections. Injecting sea-salt aerosols in sensitive areas mostly results in cloud that are located outside the sensitive areas (Fig. S27). Injecting sea-salt aerosols in the sensitive areas of SP and SA have a greater impact on the northwest. In the sensitive areas of NP, injecting sea-salt aerosols have a larger impact on the west. In the WP, the injection of sea-salt aerosols into the sensitive area does not fully reflect its susceptibility because we choose to calculate the sensitive areas away from the boundary, and the greatest susceptibilities in the WP region happens to be in the northern part of the region near the boundary.

4. Discussions and conclusions

Many studies have discussed the contributions of both the direct and indirect effects of MCB. Some studies suggest that MCB primarily relies on the indirect effects, as originally conceived, i.e., injecting aerosols to brighten clouds (Jones and Haywood, 2012; Latham et al., 2012). Other studies proposed that the direct scattering effects of aerosols may be more important (Ahlm et al., 2017; Kravitz et al., 2013; Mahfouz et al., 2023; Niemeier et al., 2013; Partanen et al., 2012). Our results indicate that the importances of both aerosol direct and indirect effects during MCB implementation depend on the injection strategies and the choice of injection regions. In cases of low sea-salt aerosol injections or the early stage of MCB implementations, changes in radiative response are mainly driven by indirect effects, causing clouds to brighten easily. As the injection of sea-salt aerosol increases, the radiative effect on clouds saturates, and the clouds are difficult to brighten. In contrast, the direct effect continues to increase linearly, leading to a subsequent decrease in the efficiencies of MCB. Partanen et al. (2012) first considered the relative importance of aerosol direct and indirect effects in MCB and preliminarily found the saturated non-linear phenomenon of indirect effects at high CDNC, as well as the linear relationships between direct effects and injection amounts. Haywood et al. (2023) also found a decrease in MCB efficiency with increasing aerosol injections. Regions initially susceptible to modification gradually became less susceptible, and aerosol direct radiation effects dominated. Other use General Circulation Model (GCM) studies also found similar results (Alterskjær and Kristjánsson, 2013; Rasch et al., 2024; Stjern et al., 2018). This study highlights and quantifies these findings in a regional model for the first time, showing the changing trends of direct and indirect effects with injection amounts in the different ocean regions. Also due to the higher resolution of the regional model, this study provides more detailed

528 cloud component changes due to sea-salt aerosol injection. The best results are obtained in regions with
529 persistent stratocumulus clouds (e.g., the oceans along the west coast of the continent), where the injected
530 sea-salt aerosols work together through both direct and indirect effects. However, in cloud-free or less
531 cloudy regions, MCB implementation can achieve the goal of reflecting more sunlight through the direct
532 scattering effect of aerosols. Considering the uncertainty in the model's resolution of clouds and the fact
533 that, in reality, the cloud distributions are also greatly influenced by the local meteorological conditions,
534 the direct scattering effects of sea-salt aerosols on MCB contributions are relatively certain. Therefore, in
535 cloud-free or less cloudy regions, the direct effect of aerosols becomes more important.

536 In the early stages of Earth-System modeling studies, the MCB processes are often simulated by
537 presetting $CDNC = 375$ or 1000 cm^{-3} in the lower regions of the ocean (Jones et al., 2009; Latham et al.,
538 2008; Rasch et al., 2009). However, many follow-up studies have suggested that injections of sea-salt
539 aerosols were difficult to produce a uniform CDNC field due to aerosol dilutions, depositions, and the
540 dependences of the spray rate on wind speed. The CDNC is highly variable spatially, and studies have
541 even reported reductions in CCN and CDNC caused by the injections of sea-salt aerosols (Alterskjær et
542 al., 2012; Korhonen et al., 2010; Pringle et al., 2012). In this study, after injecting accumulation mode
543 sea-salt aerosols at a rate of $10^{-9} \text{ kg m}^{-2} \text{ s}^{-1}$, the average CDNC concentrations for five ocean regions range
544 from 60.2 to 100 cm^{-3} , and the spatial distributions are uneven (Fig. 10 and Figs. S14–S17). Figure 9b
545 indicates that the CCNs in the five regions increase linearly ($R^2 = 1$) with increasing sea-salt aerosol
546 injections, but not all of the CCNs are converted to cloud droplets. After doubling the injection amounts,
547 the regional average CDNC is 84.8– 130 cm^{-3} , with only some grid points exceeding 200 cm^{-3} within the
548 regions. This implies that injecting more sea-salt aerosols at this point does not result in more cloud
549 droplets, and the conversion of CCN into cloud droplets is less efficient, which slows the CDNC growths
550 and tends to saturation (Fig. 9c). Alterskjær et al. (2012) similarly injected sea-salt aerosols at a rate of
551 $10^{-9} \text{ kg m}^{-2} \text{ s}^{-1}$ and found that despite emitting sea-salt mass 70 times larger than suggested by Latham et
552 al. (2008), the average CDNC over the ocean was below their assumed value of 375 cm^{-3} . This is mainly
553 due to increased competitive effects, decreased maximum supersaturations, inhibitions of aerosol
554 activations, and closures of SO_4 nucleation, resulting in reduced effectiveness of sea salt injections.
555 Notably, however, Wood (2021) found that decreased activation due to competition may be overestimated
556 in the Abdul-Razzak and Ghan activation parameterization used in many GCMs relative to a parcel model.
557 When Partanen et al. (2012) injected sea-salt aerosols in a Wind-adjusted way (injection amount different
558 from this study), they found the CDNC values of 596, 650, and 784 cm^{-3} in the NP, SP, and SA regions,

559 respectively. Injecting smaller-sized sea-salt aerosols even yields CDNC values exceeding 1000 cm^{-3} .
560 They conclude that such high values are mainly due to the model's overestimation of the sizes and
561 solubilities of accumulated mode particles, with some non-activated particles forming cloud droplets. Hill
562 and Ming (2012) increased the concentrations of sea-salt aerosols by a factor of five, resulting in an
563 average CDNC increasing from 68 to 148 cm^{-3} between $850\text{--}925 \text{ hPa}$. It is noteworthy that Hill and Ming
564 (2012) increased all modes of sea-salt aerosols. Many studies have reported that selecting the appropriate
565 injection particle size is crucial for MCB (Andrejczuk et al., 2014; Hoffmann and Feingold, 2021;
566 Partanen et al., 2012), and injecting Aitken and coarse modes may even lead to a positive forcing with
567 CDNC decreasing (Alterskjær and Kristjánsson, 2013). However, Wood (2021) argued that particles with
568 a geometric mean dry diameter of $30\text{--}60 \text{ nm}$ were most effective in brightening cloud layers, and Goddard
569 et al. (2022) similarly found that injecting Aitken mode sea-salt aerosols generated larger radiative flux
570 changes compared to accumulation mode (8.4 W m^{-2} versus 3.1 W m^{-2}). There are still considerable
571 discussions about choosing the appropriate aerosol particle sizes during the implementation of MCB, with
572 different models and parameterization schemes providing different recommendations. The sensitivity of
573 MCB to particle size is not considered in this paper and was left for future research.

574 In this study, the injection of $10^{-9} \text{ kg m}^{-2} \text{ s}^{-1}$ accumulation mode sea-salt aerosols increases cloud
575 albedo in the five ocean regions by $0.13\text{--}0.20$, with a maximum of more than 0.3 . After doubling the
576 injection amounts, the regional average cloud albedo could reach $0.45\text{--}0.55$, representing a cloud albedo
577 change of $0.15\text{--}0.24$ (Fig. 9d). These values achieve the targeted cloud albedo change as envisioned in
578 previous studies. Bower et al. (2006) suggested that to compensate for the warming associated with
579 doubling atmospheric CO_2 concentrations, a cloud albedo change of 0.16 was needed in three
580 stratocumulus cloud regions (off the west coast of Africa and North and South America, representing 3%
581 of global cloud cover). Wood (2021) proposed seeding Aitken mode particles in approximately 9% of the
582 ocean to achieve a corresponding cloud albedo increase of 0.16 . It was also suggested that injecting sea-
583 salt aerosols in a clean, undisturbed state would produce more brightening. Fig. 9d confirms this finding,
584 indicating that clouds are more likely to brighten in the early stages of sea-salt aerosol injection, and the
585 efficiency of cloud brightening decreases with increasing injection amounts. Goddard et al. (2022),
586 simulating injecting accumulation mode sea-salt aerosols in the central Gulf of Mexico, achieved a
587 simulated cloud albedo change of approximately 0.1 in the main impact region, while switching to Aitken
588 mode injection resulted in a cloud albedo change of up to 0.35 . For the global implementation of MCB,
589 global cloud albedo increases of 0.02 (Bower et al., 2006), 0.062 (Latham et al., 2008), or 0.074 (Lenton

590 and Vaughan, 2009) were estimated.

591 The contributions of the change in cloud fractions to the SW_CLD responses in this study are small,
592 which is consistent with the results of Goddard et al. (2022). However, many observational studies
593 indicate that the contribution of cloud fraction to the shortwave radiative forcing should be similar to
594 those of the CDNC and LWP (Chen et al., 2014; Rosenfeld et al., 2019). Goddard et al. (2022) believe
595 that this was due to the fact that the regional atmosphere was wetter during the simulation periods and
596 that the relative contributions of changes in cloud fraction to the SW_CLD response would be expected
597 to increase in drier months. Three of the five ocean regions in this study, SA, SP, and NP are much drier
598 and more stable than the Gulf of Mexico simulated by Goddard et al. (2022) (Fig. S28). Furthermore,
599 when we switch to conducting the experiments again in the dry months of the same year, the contribution
600 of cloud fraction to SW_CLD did not change much, remaining at ~10% (Fig. S28). We believe that this
601 might be a difference due to the parameterization scheme or resolution of the model. Liu et al. (2020)
602 simulated with WRF–Chem model and found that the cloud fraction susceptibilities to aerosols in
603 Morrison scheme and the Lin scheme were only about half of those observed by Moderate Resolution
604 Imaging Spectroradiometer (MODIS). The neglected sub-gridded clouds in the 12-km resolution
605 simulations might lead to an underestimation of the radiative effects of clouds (Yu et al., 2014). In addition,
606 cloud fractions are more commonly underestimated in the model (Glotfelty et al., 2019), and using an
607 updated parameterization scheme that accounts for sub-grid condensation might improve the model's
608 ability to resolve clouds (Zhao et al., 2023). The effects of finer resolution and more parameterization
609 schemes on aerosol-cloud interactions still need to be verified. Considering the difficulties of modeling
610 to accurately capture the effects of cloud fractions on radiation, the actual effects of MCB may be
611 underestimated.

612 This study provides quantifiable data on cloud and radiation changes for the implementation of MCB
613 over the regional oceans, and an optimization scheme on the injection strategy by adjusting the injection
614 amounts and selecting sensitive areas. It is noteworthy that different parameterization schemes, models,
615 and resolutions can influence results, especially the cloud feedback on the injected sea-salt aerosols,
616 which is a major reason for discrepancies between models (Stjern et al., 2018). In Earth-system model
617 studies, there has been a rich discussion of the climate and ecological impacts of the MCB with the same
618 framework under the Geoengineering Model Intercomparison Project (GeoMIP) (Rasch et al., 2024).
619 However, there is still a lack of a unified framework for mid-scale MCB research.

620
621

622 ***Data and code availability***

623 The computational code for cloud and radiation can be found in the code publicly available from Goddard
624 et al. (2022). The model results are available upon request.

625 ***Supplemental information.***

626 The supplementary information related to this article is available online.

627 ***Competing interests.*** The authors declare that they have no conflict of interest.

628 ***Acknowledgements.*** The study is motivated by the need to assess the susceptibility of clouds over
629 locations such as the Great Barrier Reef, where a marine cloud brightening experiment is being performed
630 by the Reef Restoration and Adaptation Program of the Southern Cross University. The authors would
631 like to thank P. B. Goddard for his open-source computing methods and codes.

632 ***Financial supports.*** This work was supported by National Natural Science Foundation of China (No.
633 42175084, 72361137007, 21577126, 41561144004), Ministry of Science and Technology of China (No.
634 2016YFC0202702, 2018YFC0213506, 2018YFC0213503) and National Air Pollution Control Key Is-
635 sues Research Program (No. DQGG0107).

636

637 **References**

638 Ahlm, L., Jones, A., Stjern, C. W., Muri, H., Kravitz, B., and Kristjánsson, J. E.: Marine cloud brightening – as effective
639 without clouds, *Atmospheric Chemistry and Physics*, 17, 13071–13087, <https://doi.org/10.5194/acp-17-13071-2017>,
640 2017.

641 Albrecht, B. A.: Aerosols, Cloud Microphysics, and Fractional Cloudiness, *Science*, 245, 1227–1230,
642 <https://doi.org/10.1126/science.245.4923.1227>, 1989.

643 Alterskjær, K. and Kristjánsson, J. E.: The sign of the radiative forcing from marine cloud brightening depends on both
644 particle size and injection amount, *Geophysical Research Letters*, 40, 210–215, <https://doi.org/10.1029/2012GL054286>,
645 2013.

646 Alterskjær, K., Kristjánsson, J. E., and Seland, Ø.: Sensitivity to deliberate sea salt seeding of marine clouds –
647 observations and model simulations, *Atmospheric Chemistry and Physics*, 12, 2795–2807, [https://doi.org/10.5194/acp-](https://doi.org/10.5194/acp-12-2795-2012)
648 [12-2795-2012](https://doi.org/10.5194/acp-12-2795-2012), 2012.

649 Andrejczuk, M., Gadian, A., and Blyth, A.: Numerical simulations of stratocumulus cloud response to aerosol
650 perturbation, *Atmospheric Research*, 140–141, 76–84, <https://doi.org/10.1016/j.atmosres.2014.01.006>, 2014.

651 Binkowski, F. S. and Roselle, S. J.: Models-3 Community Multiscale Air Quality (CMAQ) model aerosol component 1.
652 Model description, *Journal of Geophysical Research: Atmospheres*, 108, <https://doi.org/10.1029/2001JD001409>, 2003.

653 Bower, K., Chouarton, T., Latham, J., Sahraei, J., and Salter, S.: Computational assessment of a proposed technique for
654 global warming mitigation via albedo-enhancement of marine stratocumulus clouds, *Atmospheric Research*, 82, 328–

655 336, <https://doi.org/10.1016/j.atmosres.2005.11.013>, 2006.

656 Carlton, A. G. and Baker, K. R.: Photochemical Modeling of the Ozark Isoprene Volcano: MEGAN, BEIS, and Their
657 Impacts on Air Quality Predictions, *Environ. Sci. Technol.*, 45, 4438–4445, <https://doi.org/10.1021/es200050x>, 2011.

658 Chen, Y.-C., Christensen, M. W., Xue, L., Sorooshian, A., Stephens, G. L., Rasmussen, R. M., and Seinfeld, J. H.:
659 Occurrence of lower cloud albedo in ship tracks, *Atmospheric Chemistry and Physics*, 12, 8223–8235,
660 <https://doi.org/10.5194/acp-12-8223-2012>, 2012.

661 Chen, Y.-C., Christensen, M. W., Stephens, G. L., and Seinfeld, J. H.: Satellite-based estimate of global aerosol–cloud
662 radiative forcing by marine warm clouds, *Nature Geosci*, 7, 643–646, <https://doi.org/10.1038/ngeo2214>, 2014.

663 Christensen, M. W., Jones, W. K., and Stier, P.: Aerosols enhance cloud lifetime and brightness along the stratus-to-
664 cumulus transition, *Proceedings of the National Academy of Sciences*, 117, 17591–17598,
665 <https://doi.org/10.1073/pnas.1921231117>, 2020.

666 Forster, P., Ramaswamy, V., Artaxo, P., Berntsen, T., Betts, R., Fahey, D. W., Haywood, J., Lean, J., Lowe, D. C., Raga,
667 G., Schulz, M., Dorland, R. V., Bodeker, G., Etheridge, D., Foukal, P., Fraser, P., Geller, M., Joos, F., Keeling, C. D.,
668 Keeling, R., Kinne, S., Lassey, K., Oram, D., O’Shaughnessy, K., Ramankutty, N., Reid, G., Rind, D., Rosenlof, K.,
669 Sausen, R., Schwarzkopf, D., Solanki, S. K., Stenchikov, G., Stuber, N., Takemura, T., Textor, C., Wang, R., Weiss, R.,
670 Whorf, T., Nakajima, T., Ramanathan, V., Ramaswamy, V., Artaxo, P., Berntsen, T., Betts, R., Fahey, D. W., Haywood,
671 J., Lean, J., Lowe, D. C., Myhre, G., Nganga, J., Prinn, R., Raga, G., Schulz, M., and Dorland, R. V.: Changes in
672 Atmospheric Constituents and in Radiative Forcing, 2007.

673 Ghan, S. J., Liu, X., Easter, R. C., Zaveri, R., Rasch, P. J., Yoon, J.-H., and Eaton, B.: Toward a Minimal Representation
674 of Aerosols in Climate Models: Comparative Decomposition of Aerosol Direct, Semidirect, and Indirect Radiative
675 Forcing, *Journal of Climate*, 25, 6461–6476, <https://doi.org/10.1175/JCLI-D-11-00650.1>, 2012.

676 Glotfelty, T., Alapaty, K., He, J., Hawbecker, P., Song, X., and Zhang, G.: The Weather Research and Forecasting Model
677 with Aerosol–Cloud Interactions (WRF-ACI): Development, Evaluation, and Initial Application, *Mon Weather Rev*, 147,
678 1491–1511, <https://doi.org/10.1175/MWR-D-18-0267.1>, 2019.

679 Goddard, P. B., Kravitz, B., MacMartin, D. G., and Wang, H.: The Shortwave Radiative Flux Response to an Injection
680 of Sea Salt Aerosols in the Gulf of Mexico, *Journal of Geophysical Research: Atmospheres*, 127, e2022JD037067,
681 <https://doi.org/10.1029/2022JD037067>, 2022.

682 Gong, S. L.: A parameterization of sea-salt aerosol source function for sub- and super-micron particles, *Global*
683 *Biogeochemical Cycles*, 17, <https://doi.org/10.1029/2003GB002079>, 2003.

684 Grythe, H., Ström, J., Krejci, R., Quinn, P., and Stohl, A.: A review of sea-spray aerosol source functions using a large
685 global set of sea salt aerosol concentration measurements, *Atmospheric Chemistry and Physics*, 14, 1277–1297,
686 <https://doi.org/10.5194/acp-14-1277-2014>, 2014.

687 Haywood, J. M., Jones, A., Jones, A. C., and Rasch, P. J.: Climate Intervention using marine cloud brightening (MCB)
688 compared with stratospheric aerosol injection (SAI) in the UKESM1 climate model, *EGUsphere*, 1–38,
689 <https://doi.org/10.5194/egusphere-2023-1611>, 2023.

690 Hill, S. and Ming, Y.: Nonlinear climate response to regional brightening of tropical marine stratocumulus, *Geophysical*
691 *Research Letters*, 39, <https://doi.org/10.1029/2012GL052064>, 2012.

692 Hoffmann, F. and Feingold, G.: Cloud Microphysical Implications for Marine Cloud Brightening: The Importance of the
693 Seeded Particle Size Distribution, *Journal of the Atmospheric Sciences*, 78, 3247–3262, [https://doi.org/10.1175/JAS-D-](https://doi.org/10.1175/JAS-D-21-0077.1)
694 21-0077.1, 2021.

695 Horowitz, H. M., Holmes, C., Wright, A., Sherwen, T., Wang, X., Evans, M., Huang, J., Jaeglé, L., Chen, Q., Zhai, S.,
696 and Alexander, B.: Effects of Sea Salt Aerosol Emissions for Marine Cloud Brightening on Atmospheric Chemistry:
697 Implications for Radiative Forcing, *Geophysical Research Letters*, 47, e2019GL085838,
698 <https://doi.org/10.1029/2019GL085838>, 2020.

699 Janssens-Maenhout, G., Crippa, M., Guizzardi, D., Dentener, F., Muntean, M., Pouliot, G., Keating, T., Zhang, Q.,
700 Kurokawa, J., Wankmüller, R., Denier van der Gon, H., Kuenen, J. J. P., Klimont, Z., Frost, G., Darras, S., Koffi, B., and
701 Li, M.: HTAP_v2.2: a mosaic of regional and global emission grid maps for 2008 and 2010 to study hemispheric transport
702 of air pollution, *Atmospheric Chemistry and Physics*, 15, 11411–11432, <https://doi.org/10.5194/acp-15-11411-2015>,
703 2015.

704 Jones, A. and Haywood, J. M.: Sea-spray geoengineering in the HadGEM2-ES earth-system model: radiative impact and
705 climate response, *Atmospheric Chemistry and Physics*, 12, 10887–10898, <https://doi.org/10.5194/acp-12-10887-2012>,
706 2012.

707 Jones, A., Haywood, J., and Boucher, O.: Climate impacts of geoengineering marine stratocumulus clouds, *Journal of*
708 *Geophysical Research: Atmospheres*, 114, <https://doi.org/10.1029/2008JD011450>, 2009.

709 Kelly, J. T., Bhave, P. V., Nolte, C. G., Shankar, U., and Foley, K. M.: Simulating emission and chemical evolution of
710 coarse sea-salt particles in the Community Multiscale Air Quality (CMAQ) model, *Geoscientific Model Development*,
711 3, 257–273, <https://doi.org/10.5194/gmd-3-257-2010>, 2010.

712 Korhonen, H., Carslaw, K. S., and Romakkaniemi, S.: Enhancement of marine cloud albedo via controlled sea spray
713 injections: a global model study of the influence of emission rates, microphysics and transport, *Atmospheric Chemistry*
714 *and Physics*, 10, 4133–4143, <https://doi.org/10.5194/acp-10-4133-2010>, 2010.

715 Kravitz, B., Forster, P. M., Jones, A., Robock, A., Alterskjær, K., Boucher, O., Jenkins, A. K. L., Korhonen, H.,
716 Kristjánsson, J. E., Muri, H., Niemeier, U., Partanen, A.-I., Rasch, P. J., Wang, H., and Watanabe, S.: Sea spray
717 geoengineering experiments in the geoengineering model intercomparison project (GeoMIP): Experimental design and
718 preliminary results, *Journal of Geophysical Research: Atmospheres*, 118, 11,175–11,186,
719 <https://doi.org/10.1002/jgrd.50856>, 2013.

720 Kravitz, B., Wang, H., Rasch, P. J., Morrison, H., and Solomon, A. B.: Process-model simulations of cloud albedo
721 enhancement by aerosols in the Arctic, *Phil. Trans. R. Soc. A.*, 372, 20140052, <https://doi.org/10.1098/rsta.2014.0052>,
722 2014.

723 Latham, J., Rasch, P., Chen, C.-C., Kettles, L., Gadian, A., Gettelman, A., Morrison, H., Bower, K., and Choulaton, T.:
724 Global temperature stabilization via controlled albedo enhancement of low-level maritime clouds, *Philosophical*
725 *Transactions of the Royal Society A: Mathematical, Physical and Engineering Sciences*, 366, 3969–3987,
726 <https://doi.org/10.1098/rsta.2008.0137>, 2008.

727 Latham, J., Bower, K., Choulaton, T., Coe, H., Connolly, P., Cooper, G., Craft, T., Foster, J., Gadian, A., Galbraith, L.,
728 Iacovides, H., Johnston, D., Launder, B., Leslie, B., Meyer, J., Neukermans, A., Ormond, B., Parkes, B., Rasch, P., Rush,
729 J., Salter, S., Stevenson, T., Wang, H., Wang, Q., and Wood, R.: Marine cloud brightening, *Philosophical Transactions*
730 *of the Royal Society A: Mathematical, Physical and Engineering Sciences*, 370, 4217–4262,

731 <https://doi.org/10.1098/rsta.2012.0086>, 2012.

732 Latham, J., Gadian, A., Fournier, J., Parkes, B., Wadhams, P., and Chen, J.: Marine cloud brightening: regional
733 applications, *Philosophical Transactions of the Royal Society A: Mathematical, Physical and Engineering Sciences*, 372,
734 20140053, <https://doi.org/10.1098/rsta.2014.0053>, 2014.

735 Lenton, T. M. and Vaughan, N. E.: The radiative forcing potential of different climate geoengineering options,
736 *Atmospheric Chemistry and Physics*, 9, 5539–5561, <https://doi.org/10.5194/acp-9-5539-2009>, 2009.

737 Liu, F., Mao, F., Rosenfeld, D., Pan, Z., Zang, L., Zhu, Y., Yin, J., and Gong, W.: Opposing comparable large effects of
738 fine aerosols and coarse sea spray on marine warm clouds, *Commun Earth Environ*, 3, 1–9,
739 <https://doi.org/10.1038/s43247-022-00562-y>, 2022.

740 Liu, Z., Wang, M., Rosenfeld, D., Zhu, Y., Bai, H., Cao, Y., and Liang, Y.: Evaluation of Cloud and Precipitation
741 Response to Aerosols in WRF-Chem With Satellite Observations, *Journal of Geophysical Research: Atmospheres*, 125,
742 e2020JD033108, <https://doi.org/10.1029/2020JD033108>, 2020.

743 Mahfouz, N. G. A., Hill, S. A., Guo, H., and Ming, Y.: The Radiative and Cloud Responses to Sea Salt Aerosol
744 Engineering in GFDL Models, *Geophysical Research Letters*, 50, e2022GL102340,
745 <https://doi.org/10.1029/2022GL102340>, 2023.

746 Mengel, M., Nauels, A., Rogelj, J., and Schleussner, C.-F.: Committed sea-level rise under the Paris Agreement and the
747 legacy of delayed mitigation action, *Nat Commun*, 9, 601, <https://doi.org/10.1038/s41467-018-02985-8>, 2018.

748 Monahan, E. C., Spiel, D. E., and Davidson, K. L.: A Model of Marine Aerosol Generation Via Whitecaps and Wave
749 Disruption, in: *Oceanic Whitecaps: And Their Role in Air-Sea Exchange Processes*, edited by: Monahan, E. C. and
750 Niocaill, G. M., Springer Netherlands, Dordrecht, 167–174, https://doi.org/10.1007/978-94-009-4668-2_16, 1986.

751 Morrison, H., Thompson, G., and Tatarskii, V.: Impact of Cloud Microphysics on the Development of Trailing Stratiform
752 Precipitation in a Simulated Squall Line: Comparison of One- and Two-Moment Schemes, *Monthly Weather Review*,
753 137, 991–1007, <https://doi.org/10.1175/2008mwr2556.1>, 2009.

754 Niemeier, U., Schmidt, H., Alterskjær, K., and Kristjánsson, J. E.: Solar irradiance reduction via climate engineering:
755 Impact of different techniques on the energy balance and the hydrological cycle, *Journal of Geophysical Research:*
756 *Atmospheres*, 118, 11,905–11,917, <https://doi.org/10.1002/2013JD020445>, 2013.

757 Partanen, A.-I., Kokkola, H., Romakkaniemi, S., Kerminen, V.-M., Lehtinen, K. E. J., Bergman, T., Arola, A., and
758 Korhonen, H.: Direct and indirect effects of sea spray geoengineering and the role of injected particle size, *Journal of*
759 *Geophysical Research: Atmospheres*, 117, <https://doi.org/10.1029/2011JD016428>, 2012.

760 Paulot, F., Paynter, D., Winton, M., Ginoux, P., Zhao, M., and Horowitz, L. W.: Revisiting the Impact of Sea Salt on
761 Climate Sensitivity, *Geophysical Research Letters*, 47, e2019GL085601, <https://doi.org/10.1029/2019GL085601>, 2020.

762 Pleim, J. E.: A Combined Local and Nonlocal Closure Model for the Atmospheric Boundary Layer. Part I: Model
763 Description and Testing, *Journal of Applied Meteorology and Climatology*, 46, 1383–1395,
764 <https://doi.org/10.1175/jam2539.1>, 2007.

765 Pringle, K. J., Carslaw, K. S., Fan, T., Mann, G. W., Hill, A., Stier, P., Zhang, K., and Tost, H.: A multi-model assessment
766 of the impact of sea spray geoengineering on cloud droplet number, *Atmospheric Chemistry and Physics*, 12, 11647–
767 11663, <https://doi.org/10.5194/acp-12-11647-2012>, 2012.

768 Quaas, J., Boucher, O., Bellouin, N., and Kinne, S.: Satellite-based estimate of the direct and indirect aerosol climate
769 forcing, *Journal of Geophysical Research: Atmospheres*, 113, <https://doi.org/10.1029/2007JD008962>, 2008.

770 Rasch, P., Hirasawa, H., Wu, M., Doherty, S., Wood, R., Wang, H., Jones, A., Haywood, J., and Singh, H.: A protocol for
771 model intercomparison of impacts of Marine Cloud Brightening Climate Intervention, *EGUsphere*, 1–43,
772 <https://doi.org/10.5194/egusphere-2024-1031>, 2024.

773 Rasch, P. J., Latham, J., and Chen, C.-C. (Jack): Geoengineering by cloud seeding: influence on sea ice and climate
774 system, *Environ. Res. Lett.*, 4, 045112, <https://doi.org/10.1088/1748-9326/4/4/045112>, 2009.

775 Rosenfeld, Daniel, Sherwood, Steven, Wood, Robert, Donner, and Leo: Climate Effects of Aerosol-Cloud Interactions.,
776 *Science*, <https://doi.org/10.1126/science.1247490>, 2014.

777 Rosenfeld, D., Zhu, Y., Wang, M., Zheng, Y., Goren, T., and Yu, S.: Aerosol-driven droplet concentrations dominate
778 coverage and water of oceanic low-level clouds, *Science*, 363, eaav0566, <https://doi.org/10.1126/science.aav0566>, 2019.

779 Salter, S., Sortino, G., and Latham, J.: Sea-going hardware for the cloud albedo method of reversing global warming,
780 *Philosophical Transactions of the Royal Society A: Mathematical, Physical and Engineering Sciences*, 366, 3989–4006,
781 <https://doi.org/10.1098/rsta.2008.0136>, 2008.

782 Stjern, C. W., Muri, H., Ahlm, L., Boucher, O., Cole, J. N. S., Ji, D., Jones, A., Haywood, J., Kravitz, B., Lenton, A.,
783 Moore, J. C., Niemeier, U., Phipps, S. J., Schmidt, H., Watanabe, S., and Kristjánsson, J. E.: Response to marine cloud
784 brightening in a multi-model ensemble, *Atmospheric Chemistry and Physics*, 18, 621–634, <https://doi.org/10.5194/acp-18-621-2018>, 2018.

786 Stuart, G. S., Stevens, R. G., Partanen, A.-I., Jenkins, A. K. L., Korhonen, H., Forster, P. M., Spracklen, D. V., and Pierce,
787 J. R.: Reduced efficacy of marine cloud brightening geoengineering due to in-plume aerosol coagulation:
788 parameterization and global implications, *Atmospheric Chemistry and Physics*, 13, 10385–10396,
789 <https://doi.org/10.5194/acp-13-10385-2013>, 2013.

790 Twomey, S.: Pollution and the planetary albedo, *Atmospheric Environment (1967)*, 8, 1251–1256,
791 [https://doi.org/10.1016/0004-6981\(74\)90004-3](https://doi.org/10.1016/0004-6981(74)90004-3), 1974.

792 Vioni, D., Kravitz, B., Robock, A., Tilmes, S., Haywood, J., Boucher, O., Lawrence, M., Irvine, P., Niemeier, U., Xia,
793 L., Chiodo, G., Lennard, C., Watanabe, S., Moore, J. C., and Muri, H.: Opinion: The scientific and community-building
794 roles of the Geoengineering Model Intercomparison Project (GeoMIP) – past, present, and future, *Atmospheric
795 Chemistry and Physics*, 23, 5149–5176, <https://doi.org/10.5194/acp-23-5149-2023>, 2023.

796 Wang, K., Zhang, Y., Yu, S., Wong, D. C., Pleim, J., Mathur, R., Kelly, J. T., and Bell, M.: A comparative study of two-
797 way and offline coupled WRF v3.4 and CMAQ v5.0.2 over the contiguous US: performance evaluation and impacts of
798 chemistry–meteorology feedbacks on air quality, *Geoscientific Model Development*, 14, 7189–7221,
799 <https://doi.org/10.5194/gmd-14-7189-2021>, 2021.

800 Wong, D. C., Pleim, J., Mathur, R., Binkowski, F., Otte, T., Gilliam, R., Pouliot, G., Xiu, A., Young, J. O., and Kang, D.:
801 WRF-CMAQ two-way coupled system with aerosol feedback: software development and preliminary results,
802 *Geoscientific Model Development*, 5, 299–312, <https://doi.org/10.5194/gmd-5-299-2012>, 2012.

803 Wood, R.: Assessing the potential efficacy of marine cloud brightening for cooling Earth using a simple heuristic model,
804 *Atmospheric Chemistry and Physics*, 21, 14507–14533, <https://doi.org/10.5194/acp-21-14507-2021>, 2021.

805 Yu, S., Mathur, R., Pleim, J., Wong, D., Gilliam, R., Alapaty, K., Zhao, C., and Liu, X.: Aerosol indirect effect on the
806 grid-scale clouds in the two-way coupled WRF–CMAQ: model description, development, evaluation and regional
807 analysis, *Atmospheric Chemistry and Physics*, 14, 11247–11285, <https://doi.org/10.5194/acp-14-11247-2014>, 2014.

808 Zhang, K. M., Knipping, E. M., Wexler, A. S., Bhave, P. V., and Tonnesen, G. S.: Size distribution of sea-salt emissions
809 as a function of relative humidity, *Atmospheric Environment*, 39, 3373–3379,
810 <https://doi.org/10.1016/j.atmosenv.2005.02.032>, 2005.

811 Zhao, D., Lin, Y., Dong, W., Qin, Y., Chu, W., Yang, K., Letu, H., and Huang, L.: Alleviated WRF Summer Wet Bias
812 Over the Tibetan Plateau Using a New Cloud Microphysics Scheme, *Journal of Advances in Modeling Earth Systems*,
813 15, e2023MS003616, <https://doi.org/10.1029/2023MS003616>, 2023.

814 Zhao, M., Cao, L., Duan, L., Bala, G., and Caldeira, K.: Climate More Responsive to Marine Cloud Brightening Than
815 Ocean Albedo Modification: A Model Study, *Journal of Geophysical Research: Atmospheres*, 126, e2020JD033256,
816 <https://doi.org/10.1029/2020JD033256>, 2021.

817

Table 1. The cloud fraction, CDNC, LWP, and regional sea-salt aerosol concentrations at Base and after injection of sea-salt aerosols at $10^{-9} \text{ kg m}^{-2} \text{ s}^{-1}$ (Exp) for five ocean regions.

Areas	Cloud Fraction		CDNC (# cm^{-3})		LWP (g m^{-2})		Regional sea-salt aerosols ($\mu\text{g m}^{-3}$)	
	Base	Exp	Base	Exp	Base	Exp	Base	Exp
WP	0.0445	0.0488	19.3	100.0	12.8	19.8	8.91	143
NP	0.0678	0.0760	9.7	60.2	24.6	43.9	7.18	126
Equa	0.0051	0.0059	17.5	83.4	0.85	1.4	7.32	102
SP	0.0547	0.0617	11.5	89.4	21.6	38.9	6.79	176
SA	0.0519	0.0575	12.3	92.2	23.5	41.6	7.00	149

Table 2. Differences (Exp - Base) in SW_TOT, SW_CLD, SW_AER and SW_AER_CLR at the TOA due to the injection of sea-salt aerosols in different strategies in five ocean regions.

Strategies	Areas	SW_TOT (W m ⁻²)	SW_CLD (W m ⁻²)	SW_AER (W m ⁻²)	SW_AER_CLR (W m ⁻²)
Natural×5	WP	0.5	0.4	0.11	0.16
	NP	2.1	2.0	0.11	0.19
	Equa	0.07	0.01	0.06	0.07
	SP	1.7	1.6	0.08	0.14
	SA	1.4	1.3	0.11	0.16
Wind-adjusted	WP	3.8	1.9	1.9	2.3
	NP	8.4	6.8	1.6	2.4
	Equa	1.4	0.3	1.2	1.2
	SP	7.6	5.8	1.8	2.6
	SA	8.0	5.9	2.1	2.8
10 ⁻⁹ kg m ⁻² s ⁻¹	WP	18.0	4.6	13.0	15.0
	NP	23.0	13.0	9.8	15.0
	Equa	11.0	0.6	10.0	11.0
	SP	25.0	11.0	14.0	19.0
	SA	22.0	11.0	11.0	15.0
Fixed-wind-adjusted	WP	6.9	2.9	4.0	5.1
	NP	16.0	11.0	5.1	7.8
	Equa	5.0	0.5	4.5	4.7
	SP	17.0	9.9	6.6	9.8
	SA	20.0	11.0	9.1	13.0

Note: SW_TOT is upward shortwave radiative flux at the TOA for all-sky conditions. The response of SW_TOT to the sea-salt aerosols injection can be separated into the influence of the cloud radiative effect (SW_CLD, where the influence of the aerosol is excluded) and the influence of the aerosol direct scattering effect (SW_AER) in the presence of clouds. That is, $SW_TOT = SW_CLD + SW_AER$. The SW_AER_CLR is the response of aerosol direct scattering to the upward shortwave radiative flux at the TOA under clear skies.

Table 3. Relative effects of cloud fraction and albedo changes on CRF'_{param} and Twomey, LWP, and cloud fraction effects to SW_CLD responses after uniform fixed injection of 10^{-9} kg m⁻² s⁻¹ sea-salt aerosols over five ocean regions.

Areas	CRF' _{param}			Twomey Effect	$\frac{\Delta\alpha}{\Delta \ln AOD}$	
	$\alpha'_c \bar{f}$	$\bar{\alpha}_c f'$	$\alpha'_c f'$		LWP Effect	Cloud Fraction Effect
WP	71.5%	20.7%	7.82%	48.4%	41.6%	10.1%
NP	72.7%	16.9%	10.4%	48.5%	41.7%	9.71%
Equa	60.2%	27.3%	12.4%	36.4%	58.5%	5.1%
SP	73.8%	15.9%	10.3%	51.8%	39.0%	9.2%
SA	77.3%	13.9%	8.81%	52.5%	39.7%	7.8%

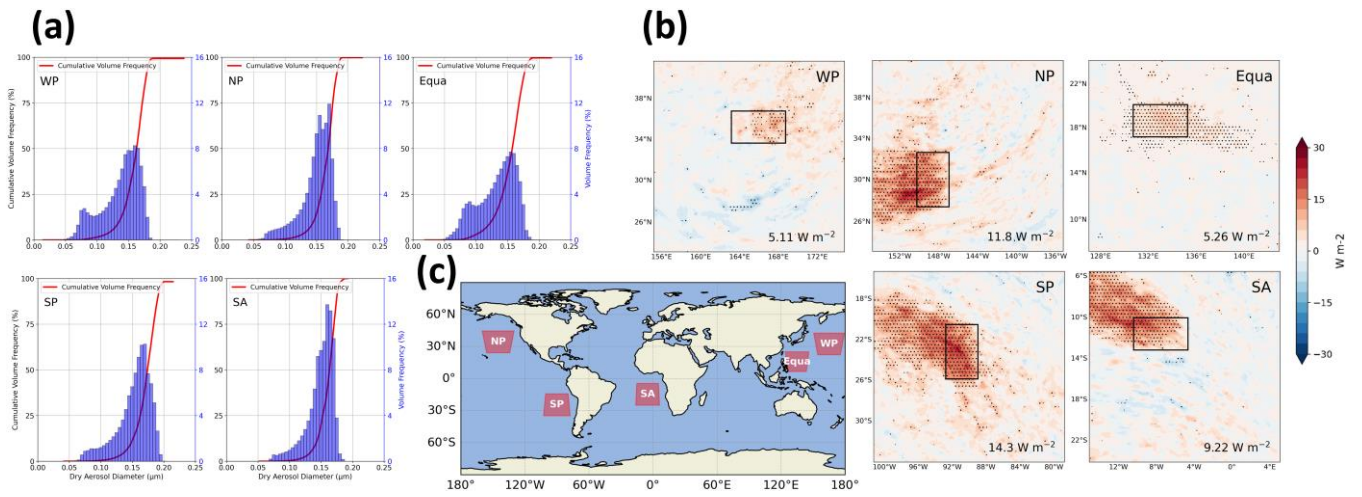


Figure 1. Injecting sea-salt aerosols into five open sea regions to simulate the implementation of MCB geoengineering. (a) The cumulative volume frequency of increased aerosol dry particle size (uniform injection of $10^{-9} \text{ kg m}^{-2} \text{ s}^{-1}$ sea-salt aerosols over the entire region). (b) Differences (Exp - Base) in the spatial distribution of the TOA upward shortwave radiative flux response (SW_TOT) resulting from uniform injection of $10^{-9} \text{ kg m}^{-2} \text{ s}^{-1}$ sea-salt aerosol in sensitive areas in five ocean regions, with SW_TOT response values resulting only in sensitive areas labeled in the lower right corner. Areas labeled with dots indicate mean differences that are significant at the 95% confidence level. Black rectangles are sensitive areas. (c) Location of the five ocean modeling domains.

Mean Liquid Cloud Fraction (from surface to 3000 m)

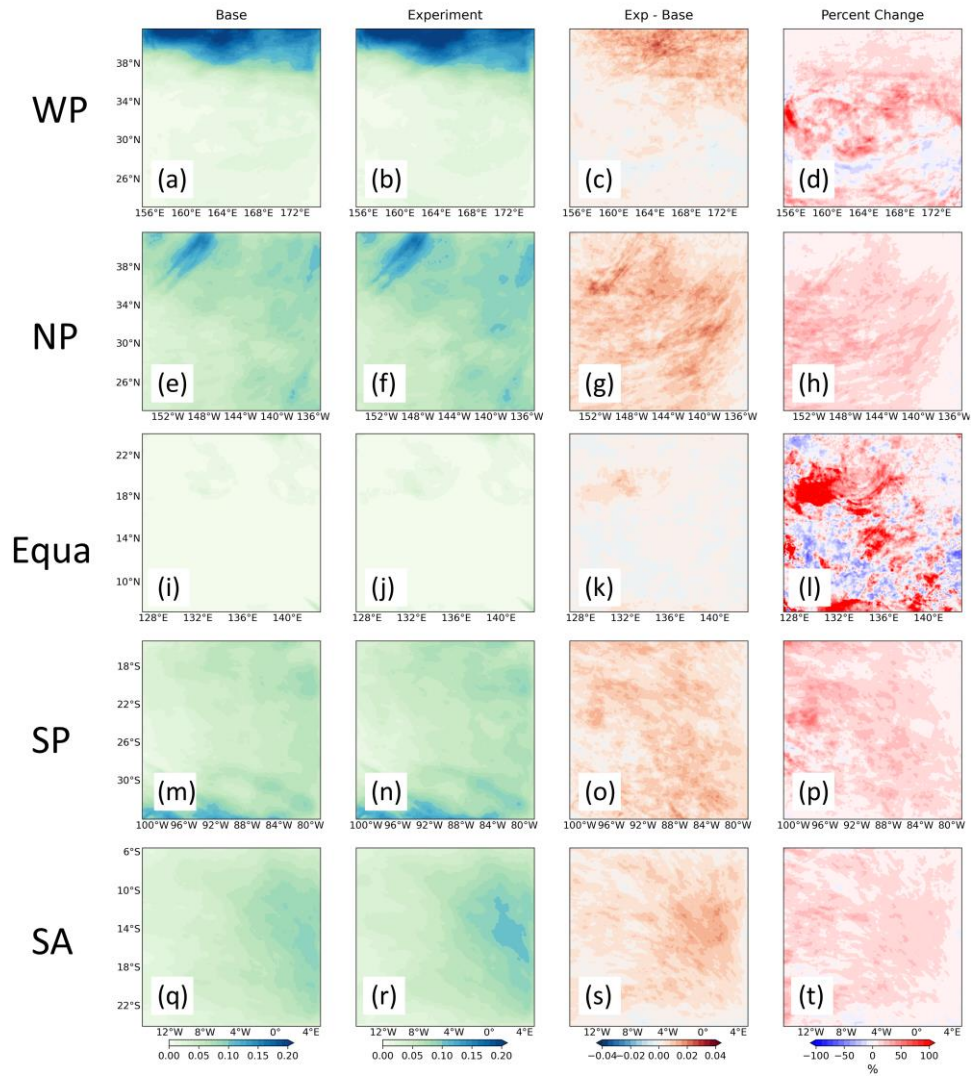


Figure 2. Column mean liquid cloud fraction from the surface to 3000 m altitude for five regions. The first to fourth columns are Base, the sensitivity experiment with a uniform injection of $10^{-9} \text{ kg m}^{-2} \text{ s}^{-1}$ sea-salt aerosols over the entire region, Exp - Base, and the percent change of Exp - Base, respectively.

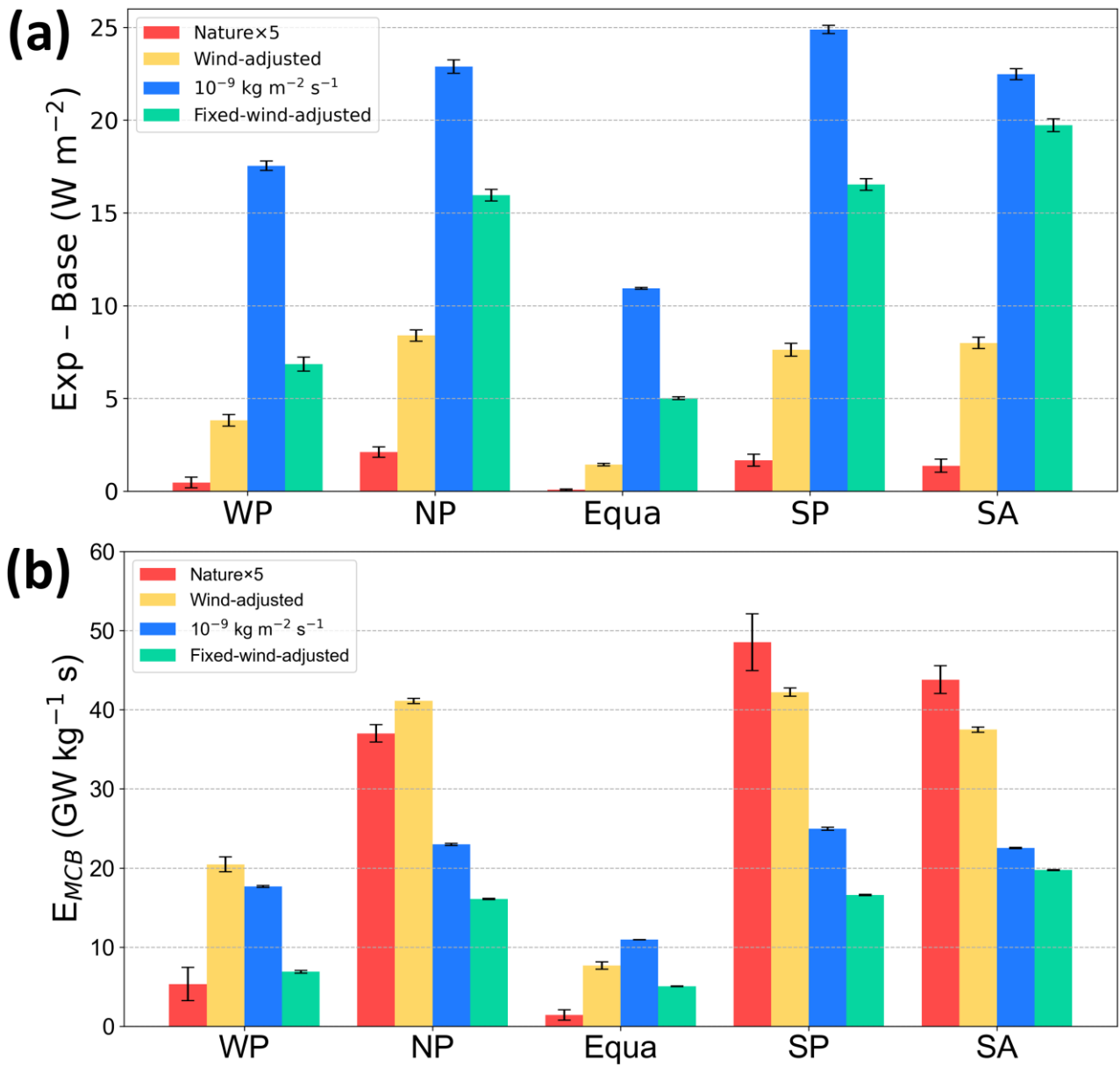


Figure 3. (a) The differences in SW_TOT and (b) the MCB efficiency (E_{MCB}) due to the injection of sea-salt aerosols in different strategies in five ocean regions.

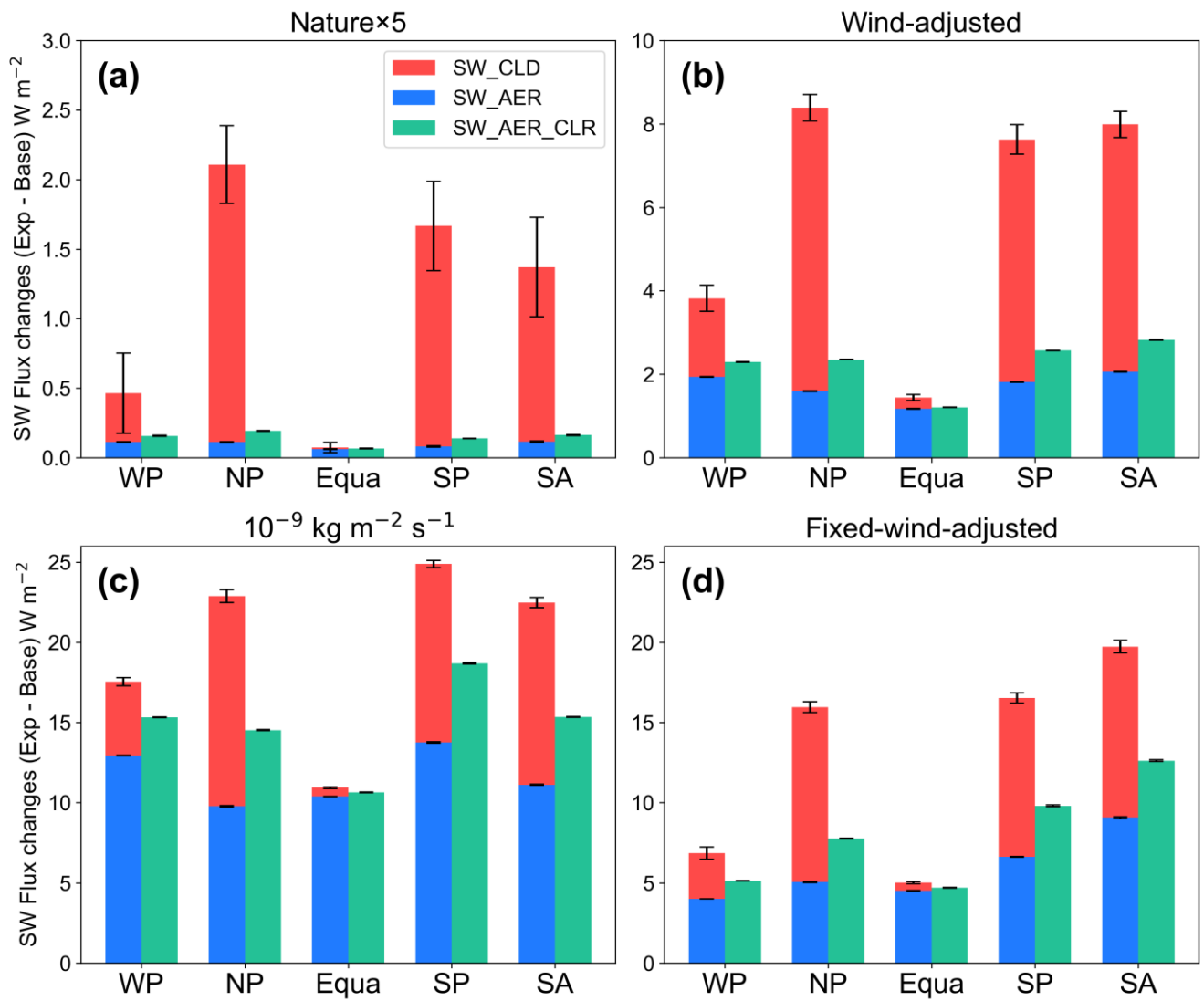


Figure 4. Decomposition of the upward shortwave radiative fluxes at the TOA due to the different strategies of injecting sea-salt aerosols in the five regions. Note that the y-axis ranges are not consistent.

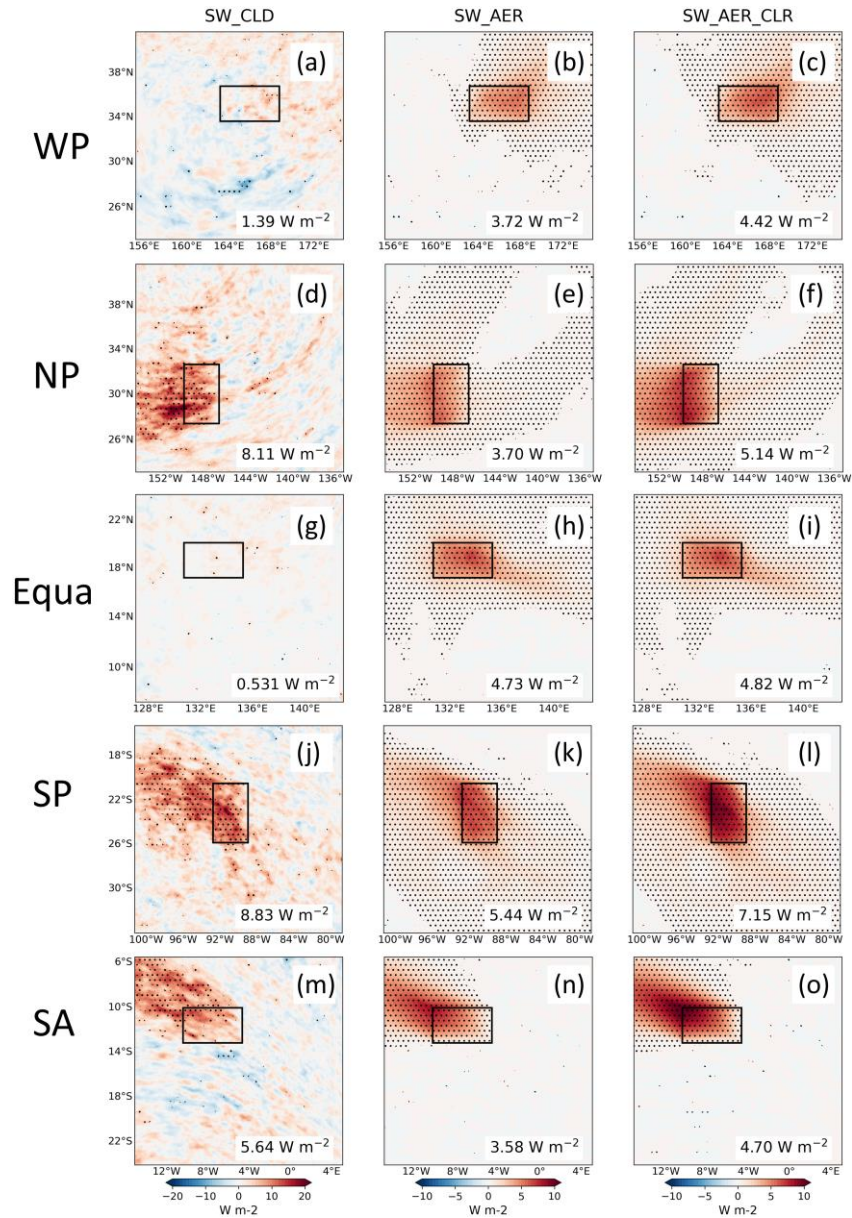


Figure 5. Spatial distribution of SW_CLD (first column), SW_AER (second column), and SW_AER_CLR (third column) responses resulting from the injection of $10^{-9} \text{ kg m}^{-2} \text{ s}^{-1}$ sea-salt aerosols in the sensitive areas over five ocean regions. The values of the radiative flux responses generated only in the sensitive area are labeled in the lower right corner. Areas labeled with dots indicate mean differences that are significant at the 95% confidence level. The black rectangles are sensitive areas.

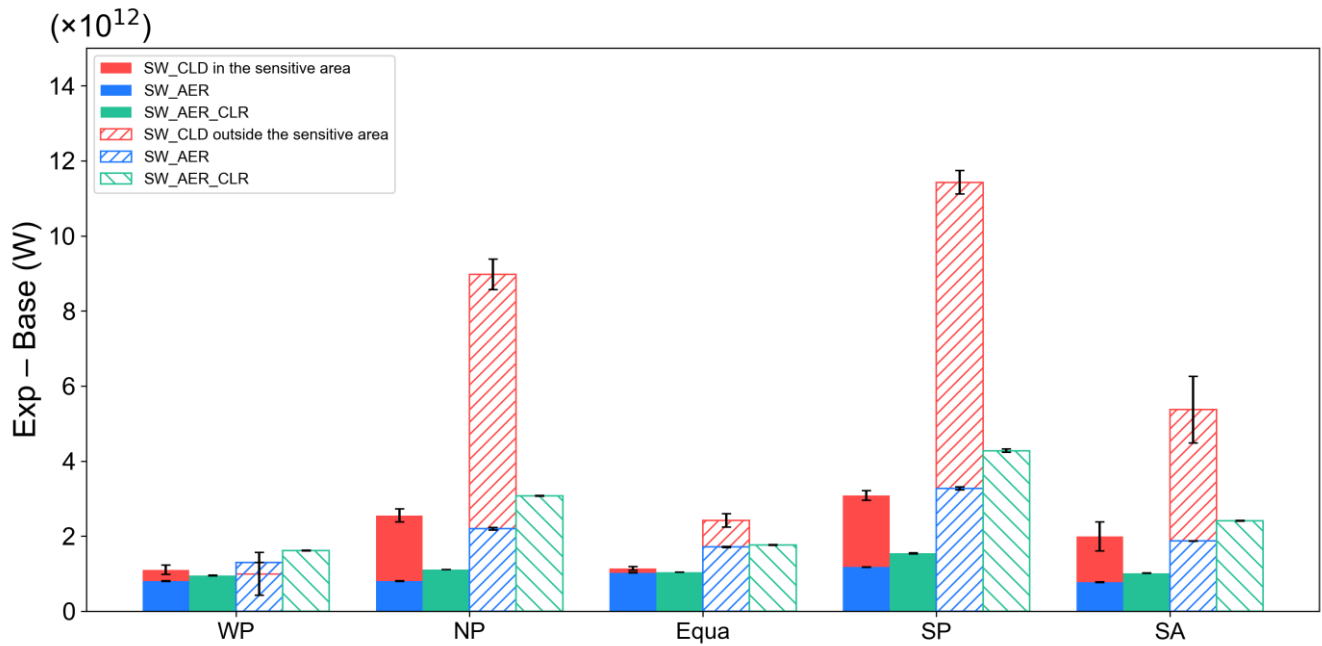


Figure 6. Total SW_CLD, SW_AER, and SW_AER_CLR responses resulting from the injection of 10^{-9} $\text{kg m}^{-2} \text{s}^{-1}$ sea-salt aerosols within the sensitive areas of the five regions. The solid columns indicate the total radiative response calculated for aerosol injection within the sensitive areas. Columns filled with hatching indicate the total radiative response outside the sensitive areas.

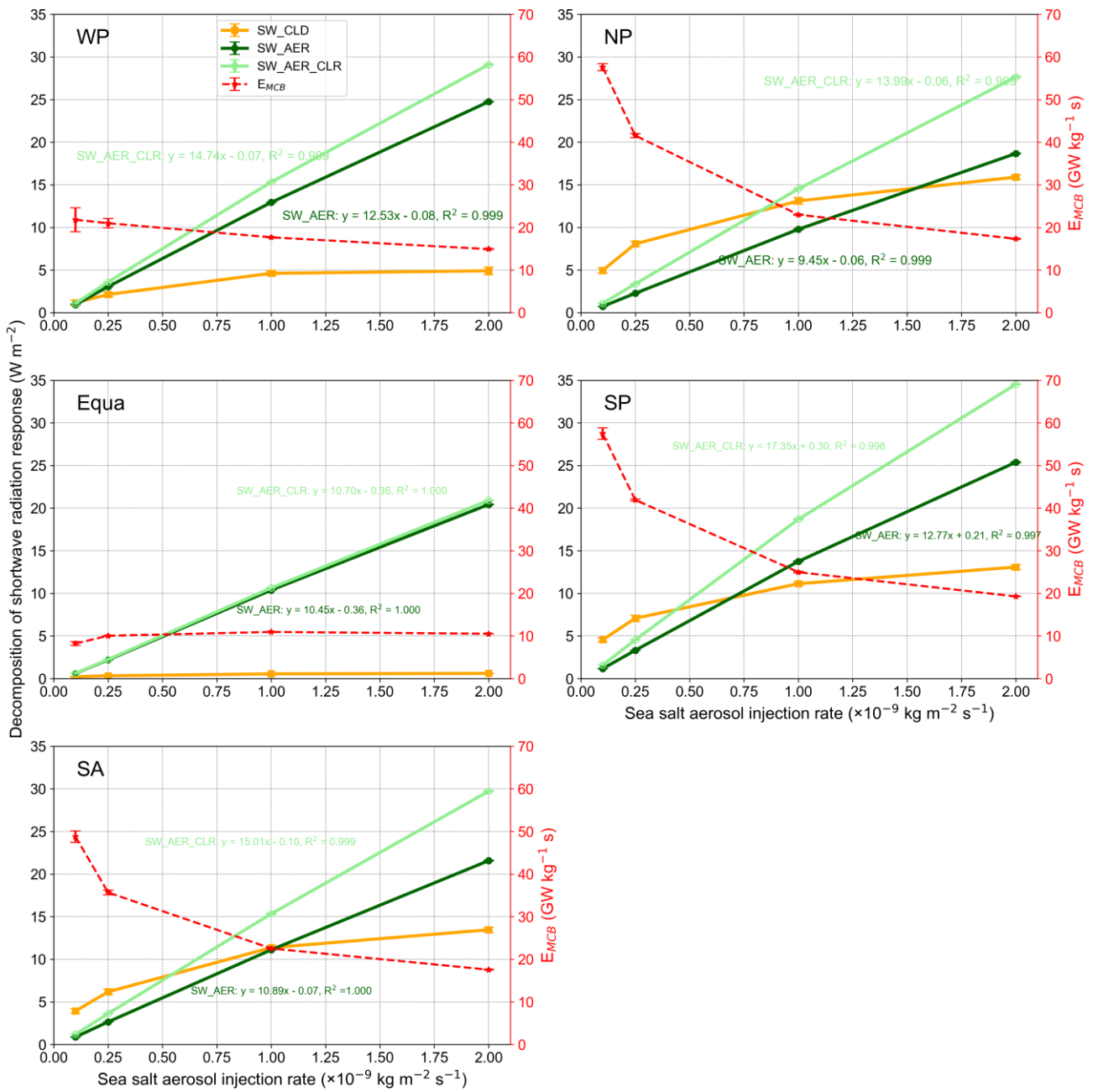


Figure 7. Changes in SW_CLD, SW_AER, and SW_AER_CLR radiative responses due to sea-salt aerosols uniformly injected in varying amounts in five ocean regions, and corresponding changes in E_{MCB} . SW_AER and SW_AER_CLR are labeled with the results of the corresponding linear regression analysis.

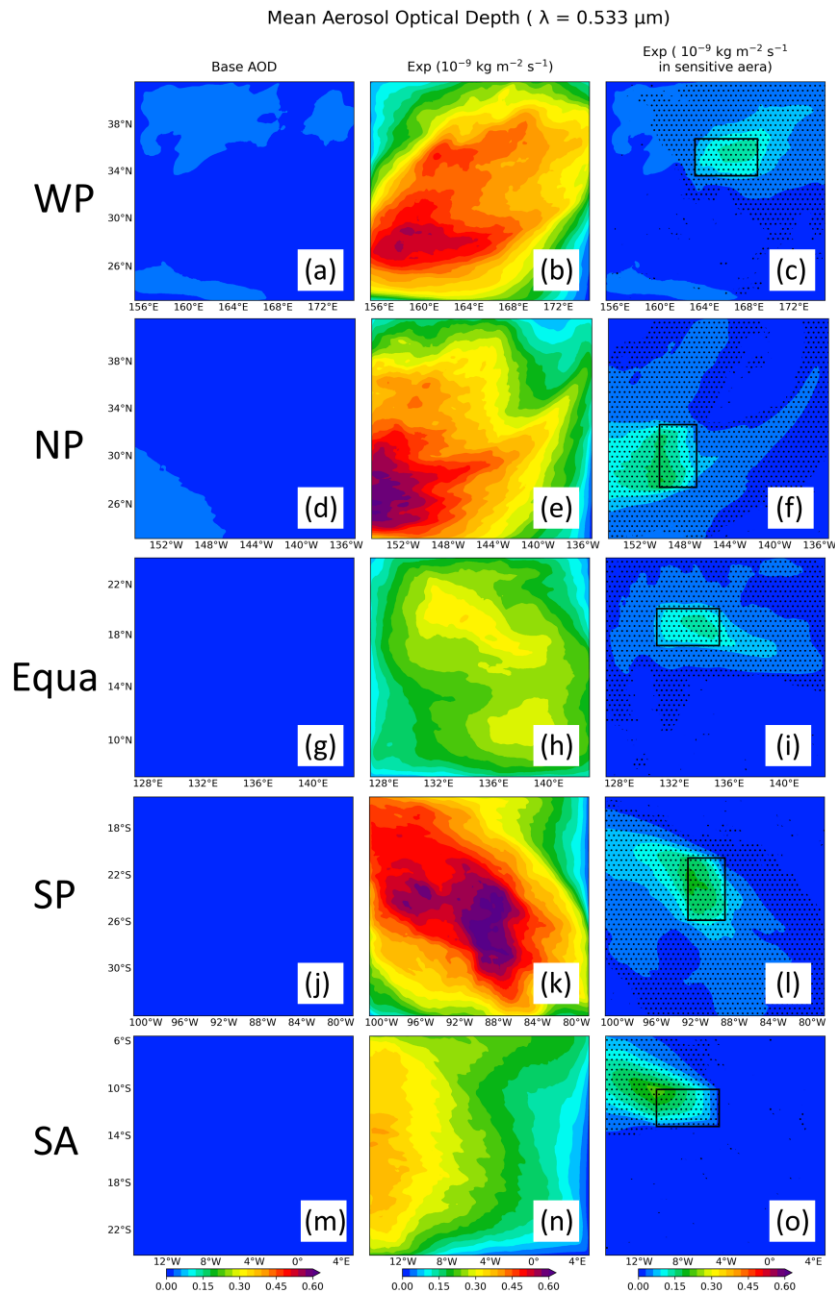


Figure 8. Spatial distribution of mean AOD ($\lambda = 0.533 \mu\text{m}$) for five ocean regions. The first column is the AOD for Base, the second column is the AOD after uniform injection at $10^{-9} \text{ kg m}^{-2} \text{ s}^{-1}$, and the third column is the AOD after uniform injection in sensitive areas. Areas labeled with dots indicate mean differences that are significant at the 95% confidence level. The black rectangles are sensitive areas.

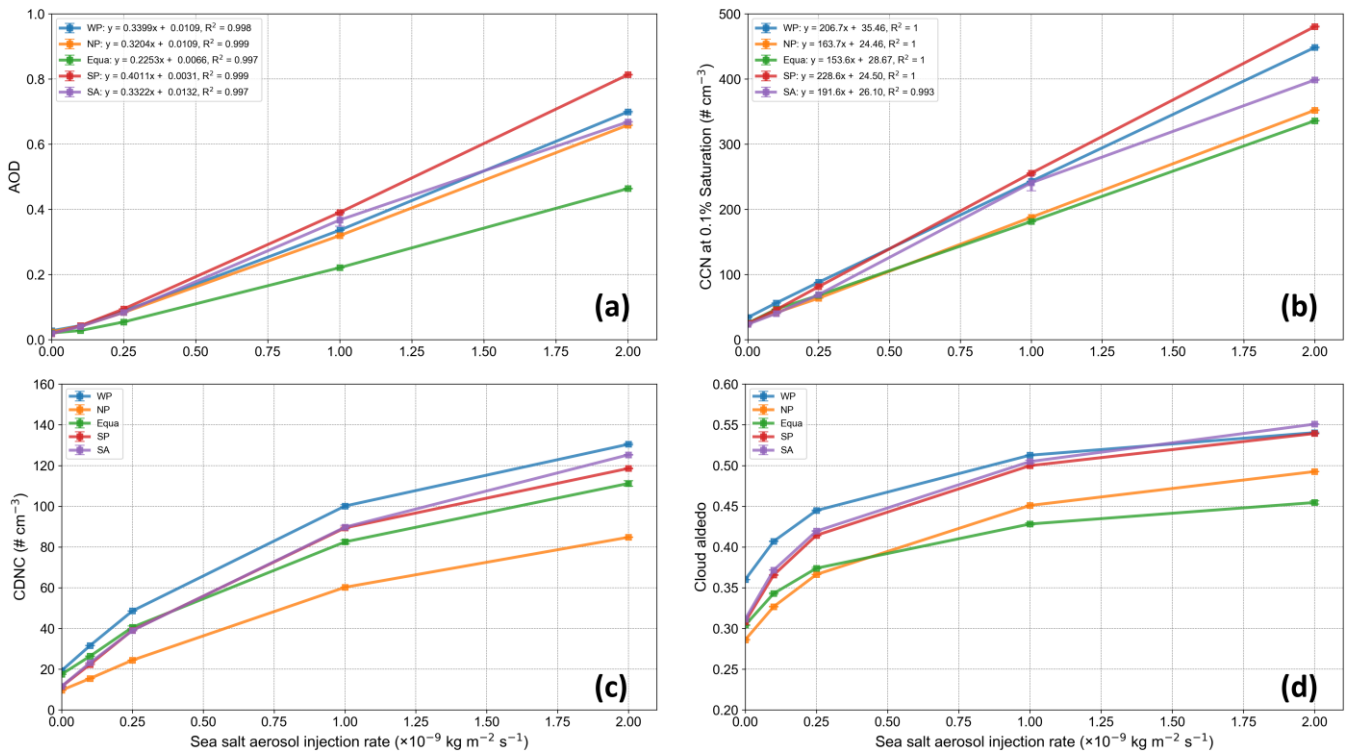


Figure 9. Relationship between changes in regional mean (a) AOD, (b) CCN, (c) CDNC, and (d) cloud albedo due to uniform injection of sea-salt aerosols across the region and the amounts of sea-salt aerosols injected. The results of the linear regression of (a) AOD and (b) CCN on the sea-salt aerosols injection amount are given at the legends.

For SP ($10^{-9} \text{ kg m}^{-2} \text{ s}^{-1}$ injection)

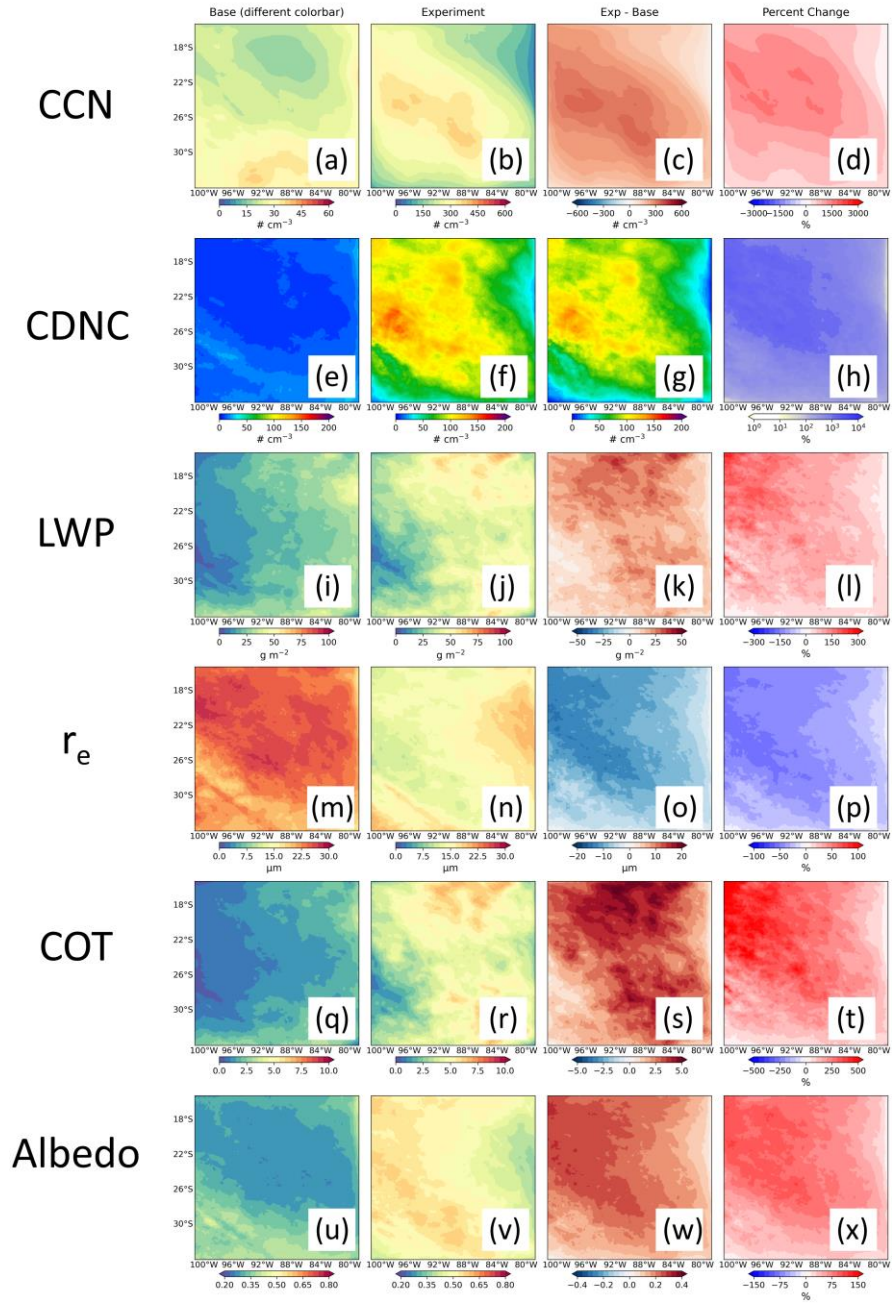


Figure 10. Spatial distribution of liquid cloud property responses after uniform injection of sea-salt aerosols with $10^{-9} \text{ kg m}^{-2} \text{ s}^{-1}$ in the SP region. Results are shown for cloud condensation nuclei (CCN, $S = 0.1\%$, $\# \text{ cm}^{-3}$), cloud droplet number concentration ($\# \text{ cm}^{-3}$), liquid water path (LWP, g m^{-2}), cloud effective radius (r_e , μm), cloud optical thickness (COT), and cloud albedo for Base (first column), Exp (second column), Exp - Base (third column), and the percentage change in Exp - Base (fourth column), respectively.

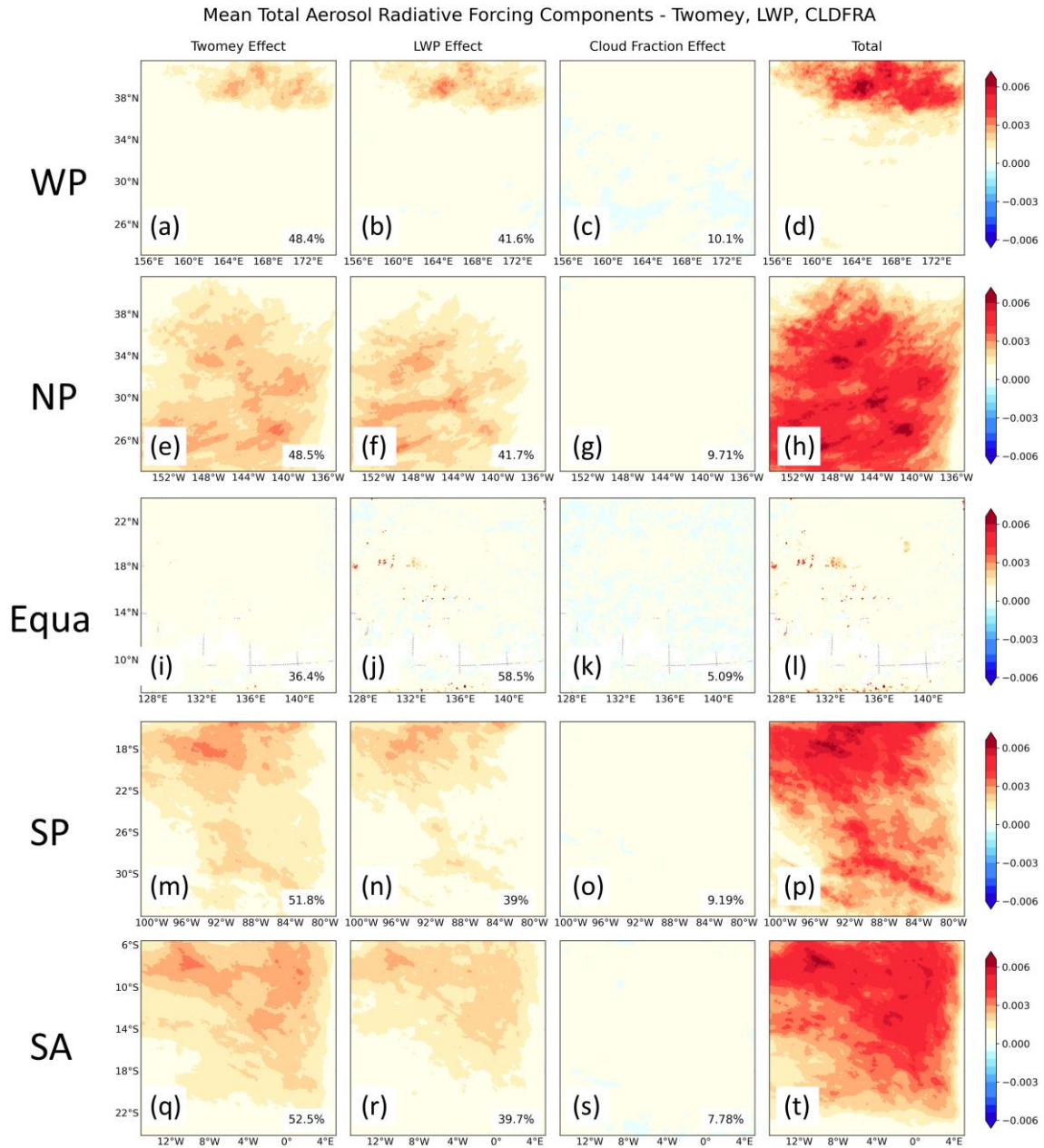


Figure 11. Spatial distribution of cloud property changes in response to SW_CLD radiation after uniform injection of sea-salt aerosols in five regions. The first column is the Twomey effect, the second column is the LWP effect, the third column is the cloud fraction effect, and the fourth column is the cloud susceptibility ($\frac{\Delta\alpha}{\Delta \ln AOD}$) to aerosol injection for the sum of the three effects. The percentage contribution of each to the total SW_CLD response over the entire region is labeled in the lower right corner.